

Supporting Information

Cobaloxime: selective nitrite reduction catalysts for tandem ammonia synthesis

Shu-Lin Meng, Chen Zhang, Chen Ye, Jia-Hao Li, Shuai Zhou, Lei Zhu, Xu-Bing Li,
Chen-Ho Tung, and Li-Zhu Wu*

*Email of corresponding author:

lzwu@mail.ipc.ac.cn

Table of Contents

1. Materials, Instruments, and Methods.....	2
2. Catalyst Synthesis and Characterization.....	7
3. Molecular eNO ₂ ⁻ RR chemistry.....	18
4. eNO ₂ ⁻ RR with Cobaloxime-modified electrodes.....	28
5. Tandem plasma N ₂ oxidation and eNO ₂ ⁻ RR.....	33
6. Reference.....	36

1. Materials, Instruments, and Methods

Materials. Dimethylglyoxime (dmg), 2,3-Butanedione monoxime ($\geq 98\%$), cobaltous chloride hexahydrate ($\text{CoCl}_2 \cdot 6\text{H}_2\text{O}$, $\geq 99\%$), 1,2-diaminobenzene, maleic acid ($\text{C}_4\text{H}_4\text{O}_4$, $\geq 99\%$), sodium nitroferricyanide(III) ($\text{C}_5\text{FeN}_6\text{Na}_2\text{O}$, $\geq 99\%$), N-(1-Naphthyl) ethylenediamine dihydrochloride ($\text{C}_{12}\text{H}_{14}\text{N}_2$, $\geq 98\%$), and sodium nitrite (NaNO_2 , $\geq 99\%$) were purchased from Innochem. Sodium phosphate monobasic (NaH_2PO_4 , $\geq 99\%$), sodium phosphate dibasic (Na_2HPO_4 , $\geq 99\%$) and hydroxylamine hydrochloride ($\text{NH}_2\text{OH} \cdot \text{HCl}$, $\geq 98\%$) were purchased from Acros. Sodium citrate monohydrate ($\text{C}_6\text{H}_5\text{Na}_3\text{O}_7 \cdot \text{H}_2\text{O}$, $\geq 99.0\%$), sodium hydroxide (NaOH , $\geq 97\%$), hydrochloric acid (HCl , $\geq 36\%$) and salicylic acid ($\text{C}_7\text{H}_6\text{O}_3$, $\geq 99\%$) were purchased from Beijing Chemical Works. Sodium hypochlorite solution (NaClO, 14.5% Cl), carbon papers (CP), multi-walled carbon nanotubes (MWCNT) and Nafion D-521 dispersion (5% wt) were purchased from Alfa Aesar. Pt plate ($1.0 \times 1.0 \text{ cm}^2$) counter electrodes and saturated calomel electrode (SCE) were purchased from Gauss Union. Millipore water ($18.2 \text{ M}\Omega \text{ cm}$) was used for all experiments. Nafion 211 membranes (DuPont) were cleaned in advance by boiling in 3% H_2O_2 for 1 h, deionized water for 1 h and then 0.5 M H_2SO_4 for 1 h, after which they were rinsed by deionized water for several times. Prior to electrode fabrication, carbon papers ($0.5 \times 2 \text{ cm}^2$) were ultra-sonically cleaned with ethanol for 3 times and then dried at $100 \text{ }^\circ\text{C}$. All other reagents were used as-received without any purifications. The $\text{Na}^{15}\text{NO}_2$ (98 atom% ^{15}N , innochem) were used for ^{15}N isotope-labelling experiments.

Physical characterizations. ^1H NMR and ^{13}C NMR spectra were recorded using a Bruker Avance DPX instrument. Mass spectra were recorded using a Trio-2000 GC-MS spectrometer. X-ray photoelectron spectroscopy (XPS) measurements were performed with ThermoFisher, ESCALAB 250Xi. Scanning electron microscopy (SEM) with elemental mapping was recorded on JEOL, JEM ARM200F. DLS was recorded on Wyatt Technology with Dybapro NanoStar OPTILAB rEX HELEOSII.

Preparation of Cobaloxime/CNT@CP electrodes. The synthesis and characterization of cobaloxime catalysts will be discussed below. Catalyst ink was prepared by dispersing 3 mg cobaloxime catalyst (Co-1~Co-10) in a 6 mL mixture solution of DMF and ethyl glycol (v/v = 1:2) with 6 mg MWCNT and 150 μL of 5wt% Nafion followed by sonication for 30 min. Then, 200 μL of the ink was drop-casted onto the $0.5 \text{ cm} \times 2 \text{ cm}$ carbon paper (CP) to cover a $0.5 \text{ cm} \times 1 \text{ cm}$ area on

both sides, and the as-prepared electrodes were dried at 50 °C for 3 h. The catalyst mass loading for all samples was 0.1 mg cm⁻².

Electrochemical measurements. Electrochemical measurements were performed with a CHI 660 E potentiostat. Molecular electrochemistry was studied in a two-chamber cell (Gauss Union) separated by a glass frit with $V = 5$ mL electrolyte, and glassy carbon (0.0705 cm² for CV and 1.00 cm² for electrolysis) was used as the working electrode, which was polished by alumina every time before use. Three-electrode configurations were adopted, where Pt plate served as the counter electrode, and SCE was used as the reference electrode. For heterogeneous cobaloxime/CNT@CP electrodes, every measurement was performed with a freshly prepared 0.5×2 cm² electrode in a H-cell separated by a Nafion 211 membrane ($V = 40$ mL catholyte). Linear sweep voltammetry (LSV) was performed at a scan rate of 5 mV s⁻¹, and under standard conditions, an Ar-saturated aqueous solution with 100 mM NaNO₂, 100 mM Na₂HPO₄, 100 mM NaH₂PO₄ and 250 mM Na₂SO₄ was used as the electrolyte (pH = 6.73). Electrolysis was performed consecutively for 7200 s under constant stirring at 240 rpm without iR-compensation, and the current densities were calculated based on the geometric area of the working electrode. All potentials were converted to RHE using the following equation:

$$E \text{ (vs. RHE)} = E \text{ (vs. SCE)} + 0.244 \text{ V} + 0.0592 \text{ V} \times \text{pH}$$

Product quantifications. After nitrite reduction, the amount of NH₄⁺ product, as well as H₂, N₂H₄, and NH₂OH as possible byproducts were measured. The NH₄⁺ leakage to the anolyte chamber of the H-cell was observed to be < 1%, which was negligible in calculating Faradic efficiencies.

Hydrogen. The amount of H₂ evolved (n_{H_2}) was monitored by gas chromatography (GC) with thermal conductivity detectors (TCD), using CH₄ as the internal standard. The faradic efficiency for H₂ evolution was calculated by:

$$FE_{H_2} = \frac{2n_{H_2}F}{Q} \times 100\%$$

where $F = 96485 \text{ C mol}^{-1}$ is the Faradic constant, Q is the charge passed during electrolysis.

Hydrazine. The amount of hydrazine was determined by the Watt-Chrisp method.¹ The color agent was prepared by dissolving 400 mg 4-(dimethylamino)benzaldehyde in 2 mL conc. H₂SO₄

and 20 mL ethanol. An 0.20 mL aliquot of the catholyte was mixed with 1.80 mL color agent, and in the presence of N_2H_4 , a yellow color would be swiftly developed within 10 min, where an absorption peak at 458 nm was observed by UV-vis spectrometer, as shown in Figure S1a. The concentration of N_2H_4 in the catholyte $c_{N_2H_4}$ follows a linear relationship with the peak absorbance, as shown in Figure S1b, and the faradic efficiency for N_2H_4 was calculated by:

$$FE_{N_2H_4} = \frac{10c_{N_2H_4}VF}{Q} \times 100\%$$

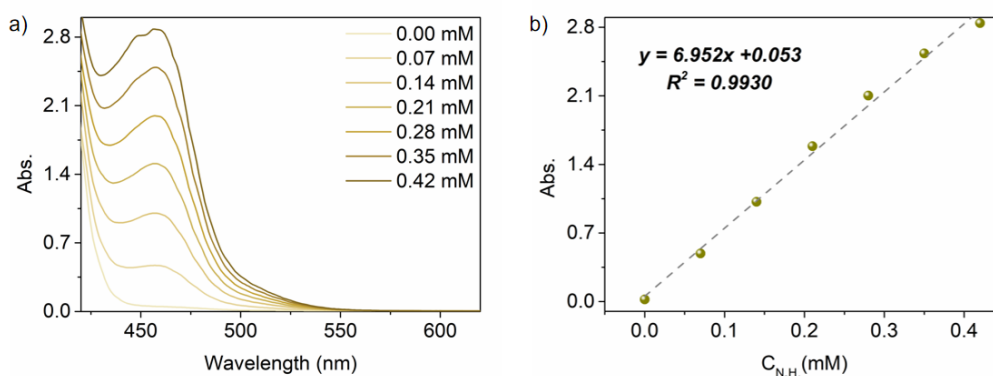


Figure S1. determination of N_2H_4 by Watt-Chrisp method.

Hydroxylamine. To quantify NH_2OH , the following literature procedures were executed:² to 1.00 mL of the catholyte was added 1.00 mL PBS buffer and 1.00 mL 1% 8-hydroxylquinoline. Under vigorous shaking, 1.00 mL 0.1 M Na_2CO_3 was added and the mixture was heated at 100 °C for 1 min. In the presence of NH_2OH , the solution would turn from light yellow to blue-green, showing an absorption peak at ~705 nm (Figure S2a). Plotting the peak absorbance with NH_2OH concentration in the catholyte c_{NH_2OH} yielded a calibration curve in Figure S2b, and the faradic efficiency for NH_2OH was calculated by:

$$FE_{NH_2OH} = \frac{4c_{NH_2OH}VF}{Q} \times 100\%$$

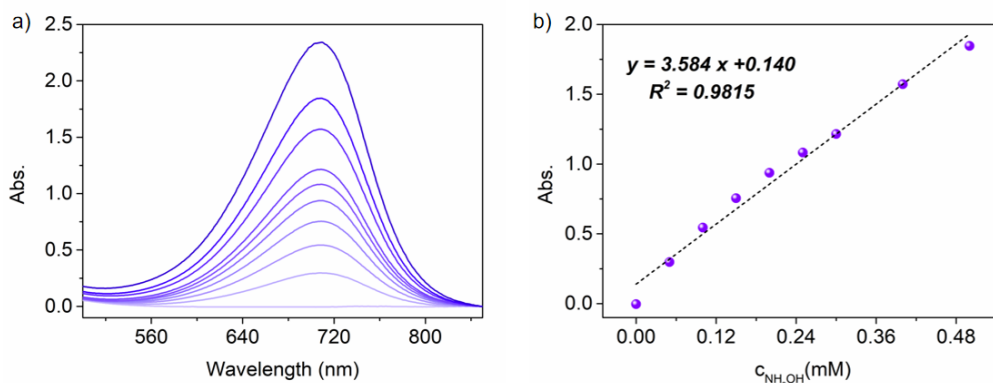


Figure S2. determination of NH_2OH by Watt-Chrisp method.

Ammonium. In this work, both indophenol-blue method and ^1H NMR were employed to quantify ammonia, and their consistent results with each other at least 5 times far above ambient background levels ($<0.05 \times 10^{-3}$ mol/L) verified successful ammonia synthesis. In indophenol-blue method, an aliquot of the catholyte was first diluted by n times to a proper concentration, typically at $\sim 0.5 \times 10^{-3}$ mol/L and 0.20 mL of the diluted solution was mixed sequentially with 0.60 mL solution A (2.00 g salicylic acid, 2.00 g sodium citrate monohydrate and 2.80 g KOH dissolved in 40 mL DI water), 0.60 mL solution B (0.425 mL NaClO with 14.5% Cl and 2.24 g KOH in 40 mL DI water) and 0.60 mL solution C (0.40 g sodium nitroferricyanide in 40 mL DI water). In the presence of NH_4^+ , the color changed gradually from yellow to green and stabilized in 60 min. An absorption peak at ~ 660 nm emerged, and the peak absorbance followed an excellent linear relationship with $c_{\text{NH}_4^+}$.

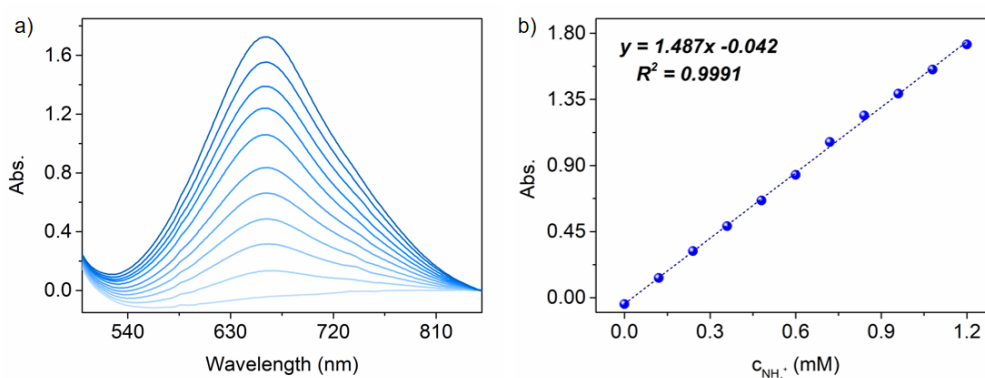


Figure S3. determining NH_4^+ in $10^{-4} \sim 10^{-3}$ mol/L using indophenol-blue method.

In ^{15}N -isotope labelling experiments and long-hour electrolysis, ammonia detection was conveniently performed by ^1H NMR.³ Briefly, 50 μL of the catholyte was acidified by 50 μL 4 M HCl with 20 mM maleic acid ($\text{C}_4\text{H}_4\text{O}_4$) as the internal standard. The mixture then was dissolved in

550 μL DMSO- d_6 and subjected to 400 MHz ^1H NMR. After 128 scans, $^{14}\text{NH}_4^+$ gave well-defined triplet at 7.31 ppm with $J = 72$ Hz while $^{15}\text{NH}_4^+$ displayed a doublet with $J = 52$ Hz (Figure S4). The peak ratio between NH_4^+ and maleic acid (6.25 ppm) obeyed good linear relationship with ammonia concentrations.

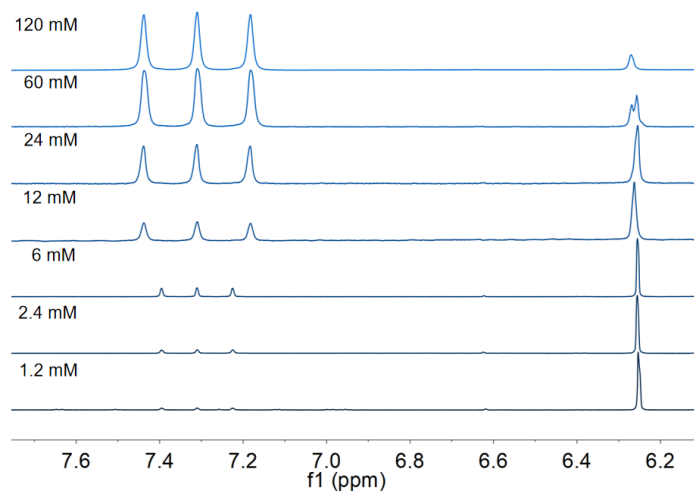


Figure S4. Quantifying NH_4^+ with ^1H NMR, using 20 mM maleic acid as internal standard.

With $c_{\text{NH}_4^+}$ determined by either indophenol-blue or ^1H NMR method, the faradic efficiency for ammonia synthesis in NO_2^- reduction was determined by:

$$FE_{\text{NH}_4^+} = \frac{6nc_{\text{NH}_4^+}VF}{Q} \times 100\%$$

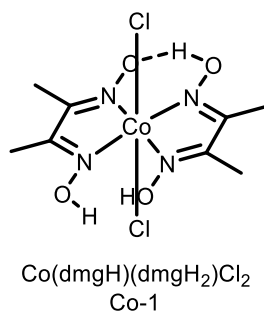
The reduction of NO to ammonia consumes 5 electrons, and in this case,

$$FE_{\text{NH}_4^+} = \frac{5nc_{\text{NH}_4^+}VF}{Q} \times 100\%$$

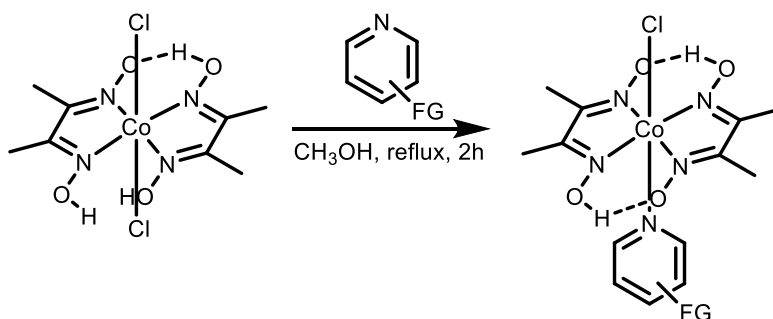
In NH_2OH reduction, the formation of ammonia is a $2e^-$ process, so its Faradic efficiency is calculated by

$$FE_{\text{NH}_4^+} = \frac{2nc_{\text{NH}_4^+}VF}{Q} \times 100\%$$

2. Catalyst Synthesis and Characterization



Co(dmgH)(dmgH₂)Cl₂ (Co-1): same as literature reports, and the obtained ¹H NMR and ESI-MS were consistent with literature.⁴



Co(dmgH)₂(FG-Py)Cl (Co-2~Co-8): according to literature,⁵ Co-2~Co-8 were synthesized by refluxing 0.50 mmol (180 mg) Co-1 and 0.50 mmol axial FG-Py ligand in methanol for 2 h under air. The mixtures were then cooled down to room temperature, when yellow-brown precipitates formed. The precipitates were filtered, washed with cold methanol and diethyl ether and dried.

Co-2 (FG = H): 268 mg brown solid, yield 64 %. ¹H NMR (400 MHz, DMSO-d₆) δ 18.44 (s, 2H), 8.02 (d, *J* = 5.8 Hz, 2H), 7.88 (t, *J* = 7.6 Hz, 1H), 7.45 (t, *J* = 6.8 Hz, 2H), 2.30 (s, 12H), which was consistent with literature.⁶

Co-3 (FG = 4-OH): 232 mg brown solid, yield 54 %. ¹H NMR (400 MHz, DMSO-d₆) δ 18.45 (s, 2H), 8.02 (d, *J* = 6.8 Hz, 2H), 7.86 (t, *J* = 7.4 Hz, 1H), 7.46 (t, *J* = 6.5 Hz, 2H), 2.30 (s, 12H), which agreed with literature.⁵

Co-4 (FG = 4-SH): 311 mg yellow solid, yield 72 %. ¹H NMR (400 MHz, DMSO-d₆) δ 18.47 (s, 2H), 7.22 (d, *J* = 6.5 Hz, 1H), 6.81 (s, 2H), 6.34 (d, *J* = 6.5 Hz, 2H), 2.29 (s, 12H), consistent with

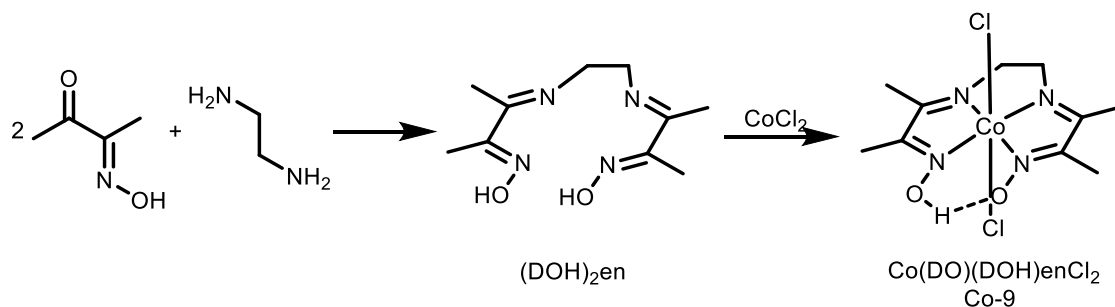
literature reports.⁵

Co-5 (FG = 4-COOH): 157 mg yellow solid, yield 34 %. ¹H NMR (400 MHz, DMSO-*d*₆) δ 18.46 (s, 2H), 8.21-8.13 (m, 2H), 7.87 (d, *J* = 5.9 Hz, 2H), 2.33 (s, 12H), in line with literature reports.⁷

Co-6 (FG = 4-CONH₂): 216 mg yellow solid, yield 47 %. ¹H NMR (400 MHz, DMSO-*d*₆) δ 11.40-10.60 (br, 2H), 8.94 (d, *J* = 5.5 Hz, 2H), 8.48 (s, 1H), 8.23-8.10 (m, 2H), 8.02 (s, 1H), 2.33 (s, 12H), which corresponded with literature reports.⁸

Co-7 (FG = 3-COOH): 262 mg yellow solid, yield 57 %. ¹H NMR (400 MHz, DMSO-*d*₆) δ 18.69-18.04 (br, 2H), 8.61 (s, 1H), 8.32 (d, *J* = 7.9 Hz, 1H), 8.20 (d, *J* = 5.8 Hz, 1H), 7.62 (t, *J* = 6.9 Hz, 1H), 2.32 (s, 12H), which corresponded with literature reports.⁹

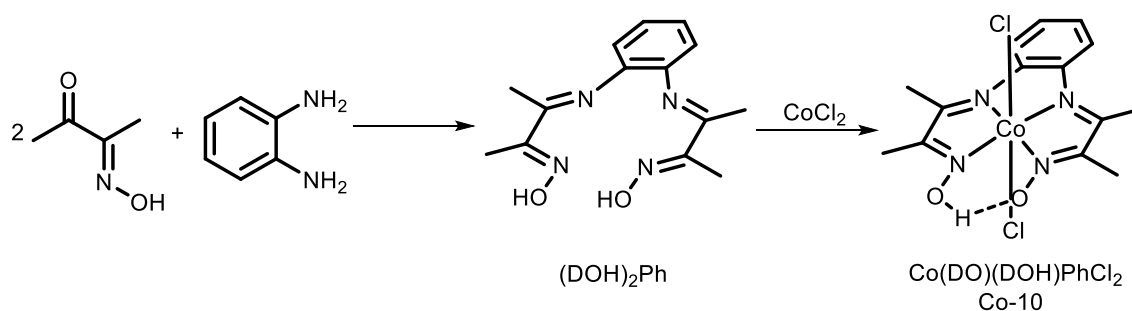
Co-8 (FG = 3-CONH₂): 234 mg yellow solid, yield 61 %. ¹H NMR (400 MHz, DMSO-*d*₆) δ 11.0-10.10 (br, 2H), 9.18 (s, 1H), 8.91 (d, *J* = 5.6 Hz, 1H), 8.66 (dt, *J* = 8.1, 1.8 Hz, 1H), 8.55-8.20 (m, 1H), 8.07-7.70 (m, 2H), 2.33 (s, 12H), which corresponded with literature reports.⁸



Co(DO)(DOH)enCl₂ (Co-9): according to literature with slight modifications,¹⁰ we synthesized the (DOH)₂en ligand first and then coordinated it with CoCl₂·6H₂O. Briefly, to 606 mg 2,3-butanedione monoxime (6.00 mmol) dissolved in 15 mL methanol, 200 μL ethylenediamine (3.00 mmol) was swiftly injected. The mixture was stirred at room temperature, and after 1 h 45 min, a white solid was formed. The solid was filtered, washed with dichloromethane and dried under vacuum to give 413 mg (DO)(DOH)en ligand. Yield 61%. ¹H NMR (400 MHz, DMSO-*d*₆) δ 11.44 (s, 2H), 3.70 (s, 4H), 2.02 (s, 6H), 1.89 (s, 6H), which agreed well with literature results.

The (DOH)₂en ligand (226 mg, 1.00 mmol) and cobaltous chloride hexahydrate (238 mg, 1.00 mmol) were mixed in 25 mL acetone and stirred at room temperature for 16 h. A yellow-green solid was formed, which was filtered and washed with acetone. Yield 41% (145 mg). ¹H NMR (400 MHz, DMSO-*d*₆) δ 4.68 (s, 2H), 2.60 (s, 4H), 2.41 (s, 6H), 2.09 (s, 6H). ESI M⁺ calc. 285.0639. found

285.0642, which agreed with literature reports.¹¹



Co(DO)(DOH)PhCl₂ (Co-10): Co-10 was also synthesized by ketone-diamine condensation to make the (DOH)₂Ph ligand followed by metallization. In synthesizing the (DOH)₂Ph ligand, 606 mg 2,3-butanedione monoxime (6.00 mmol) and 324 mg 1,2-diaminobenzene (3.00 mmol) were mixed in 15 mL water and heated to reflux. An orange precipitate gradually formed after 4 hours and then the mixture was cooled to 4 °C overnight. The precipitate was filtered, washed with cold water and dried under vacuum to afford 394 mg brown solid. Yield: 87%. ¹H NMR (400 MHz, DMSO-*d*₆) δ 11.37 (s, 2H), 7.96 (dt, *J* = 6.8, 3.1 Hz, 2H), 7.72 (dd, *J* = 6.5, 3.4 Hz, 2H), 2.68 (s, 6H), 1.92 (s, 6H). ¹³C NMR (101 MHz, DMSO-*d*₆) 153.9 153.0 140.4 128.7 128.0 22.7 9.3, which was consistent with literature.

The (DOH)₂Ph ligand (274 mg, 1.00 mmol) and cobaltous chloride hexahydrate (238 mg, 1.00 mmol) were mixed in 10 mL ethanol and refluxed for 3 h. Using Et₂O as the non-solvent, it was crystallized to form a green solid. Yield 87% (350 mg). ¹H NMR (400 MHz, DMSO-*d*₆) δ 8.12 (dd, *J* = 6.2, 3.5 Hz, 2H), 7.88 (dd, *J* = 6.4, 3.5 Hz, 2H), 2.84 (s, 6H), 2.68 (s, 6H), which was consistent with literature reports.¹¹

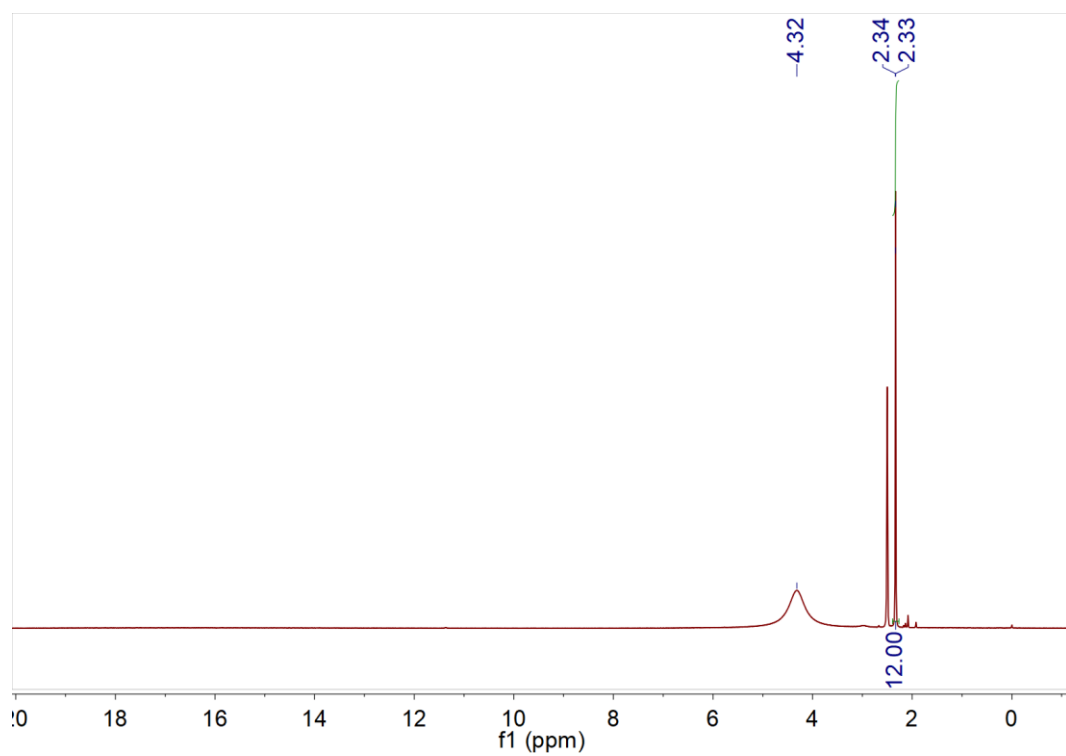


Figure S5. ^1H NMR of Co-1 in DMSO-d_6 .

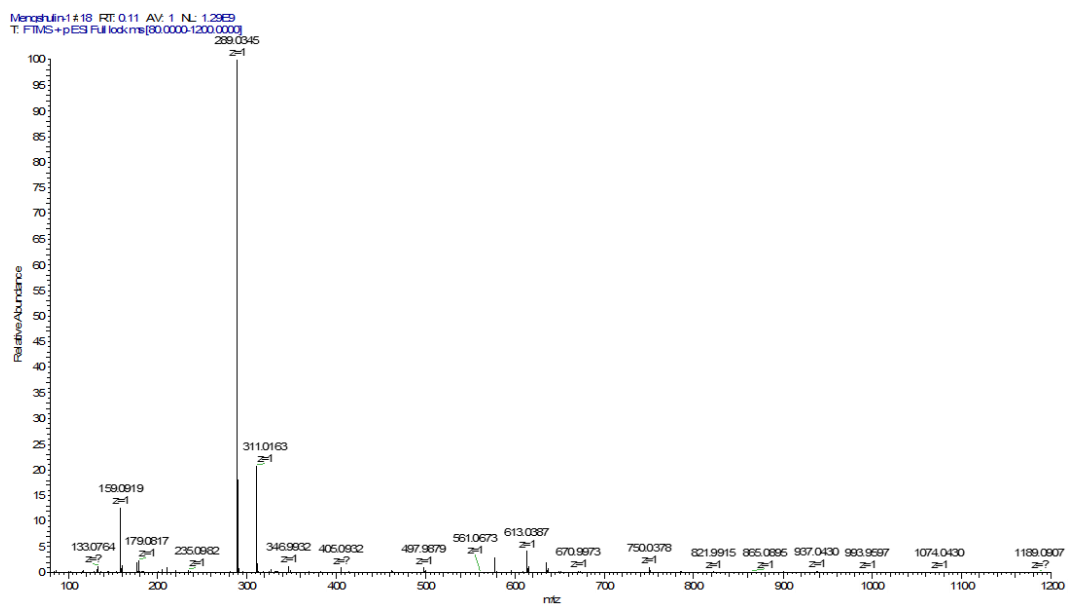


Figure S6. ESI-MS of Co-1.

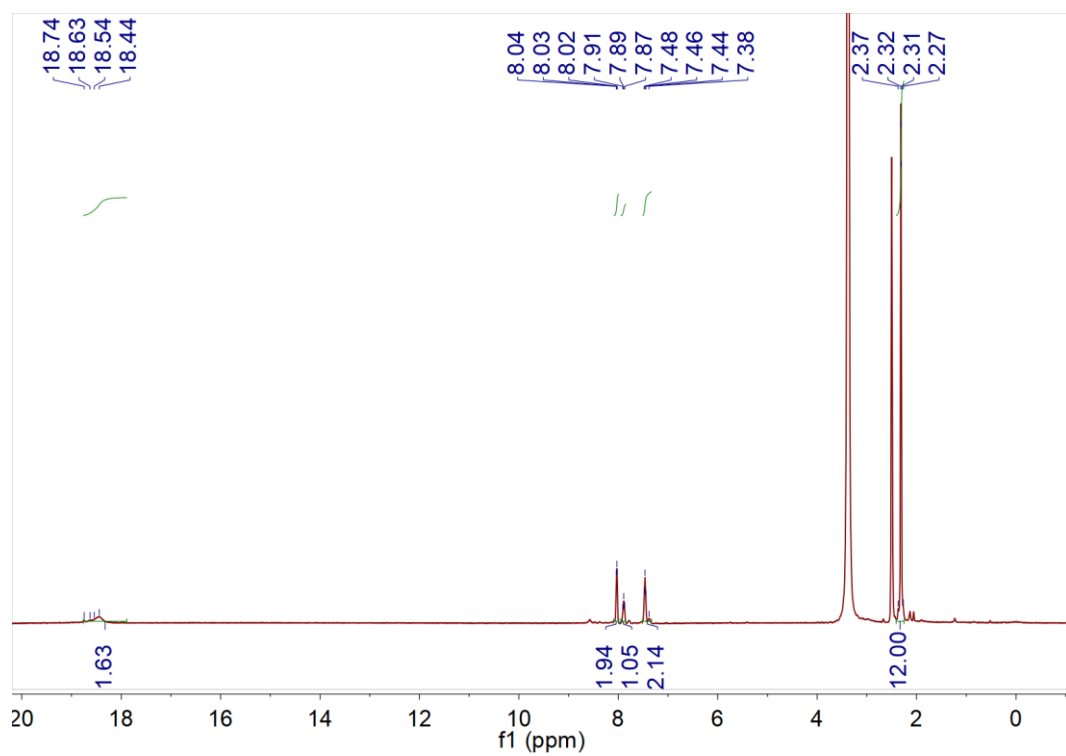


Figure S7. ^1H NMR of Co-2 in DMSO-d_6 .

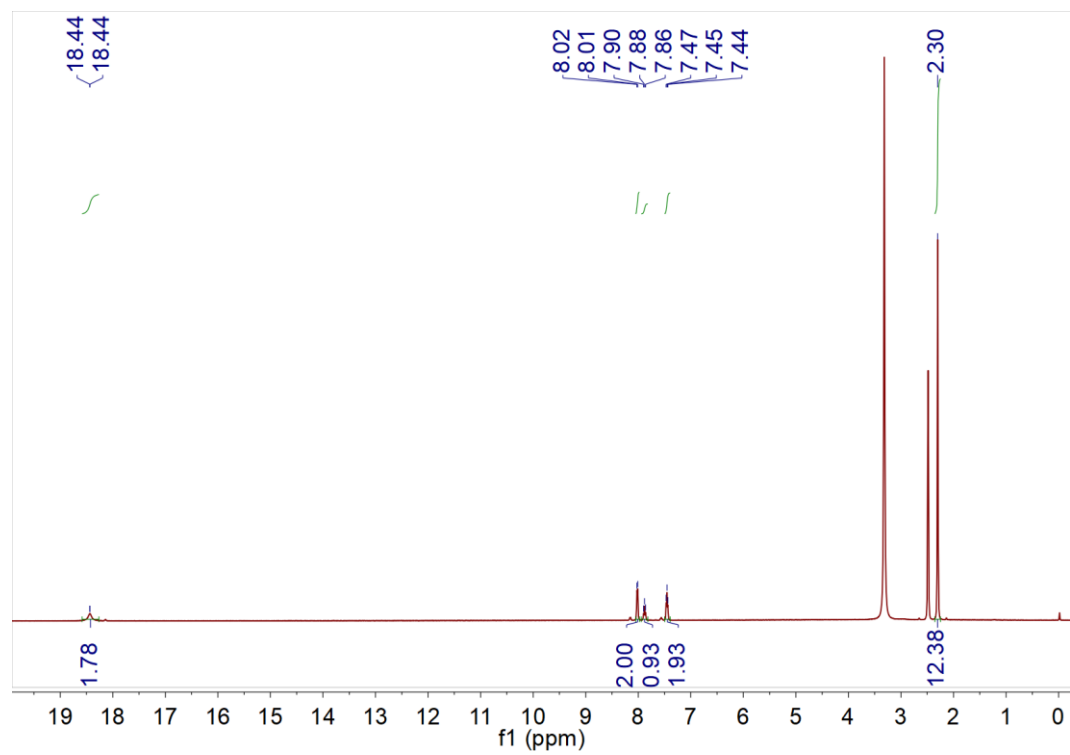


Figure S8. ^1H NMR of Co-3 in DMSO-d_6 .

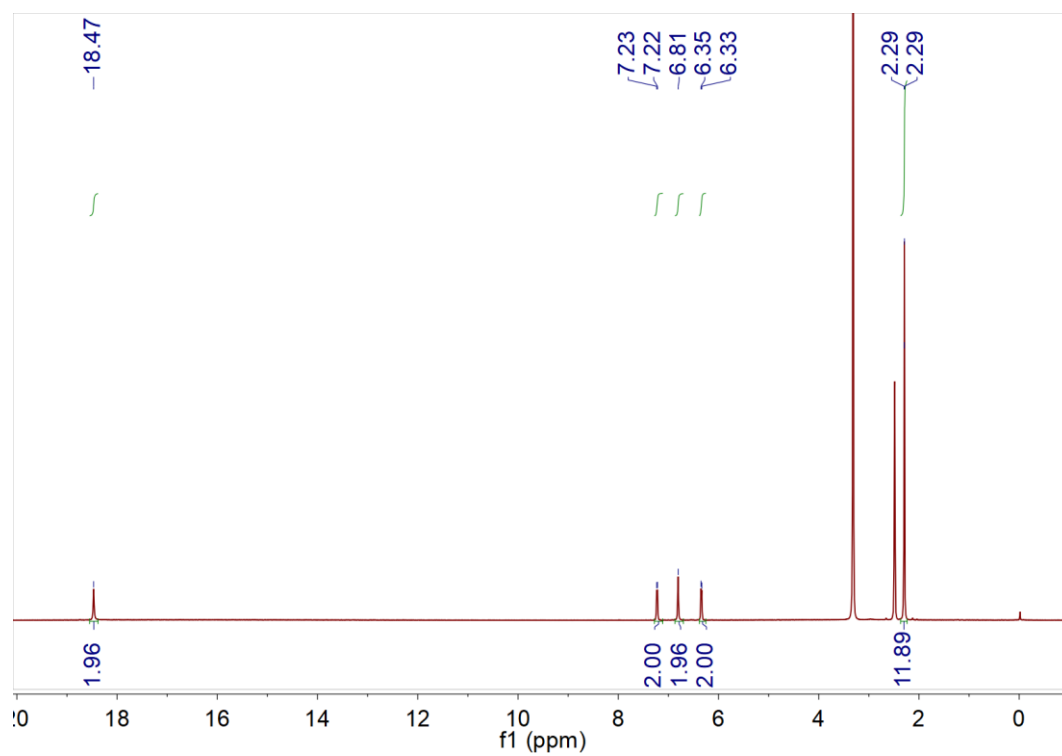


Figure S9. ^1H NMR of Co-4 in DMSO-d_6 .

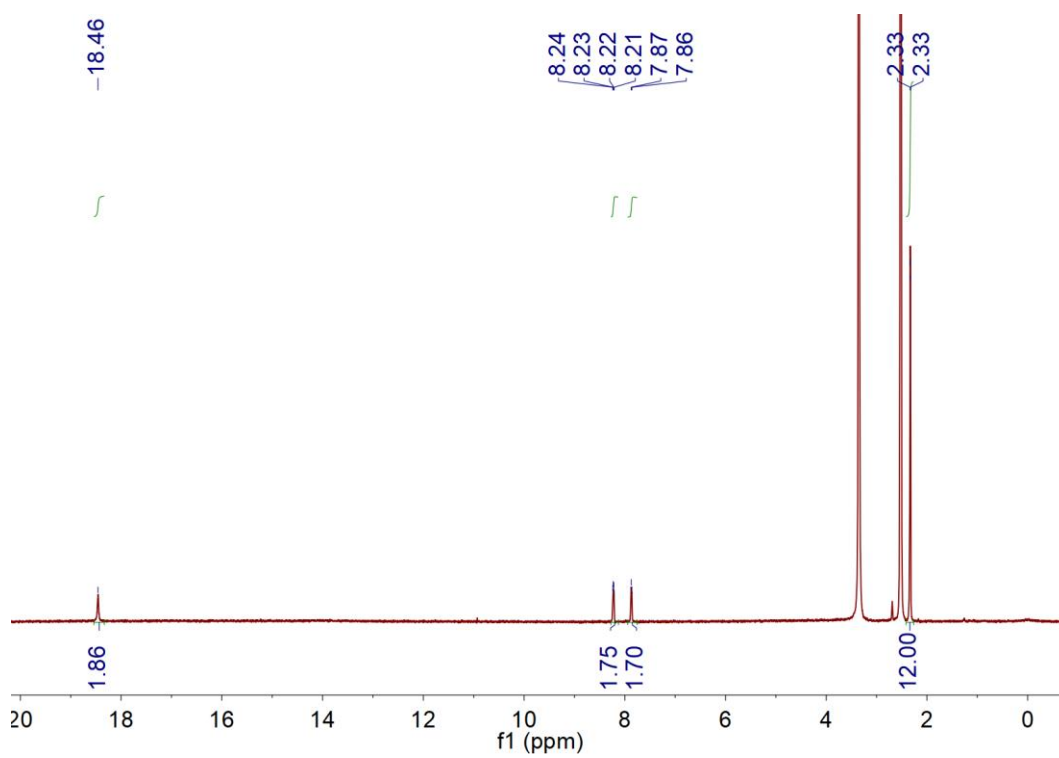


Figure S10. ^1H NMR of Co-5 in DMSO-d_6 .

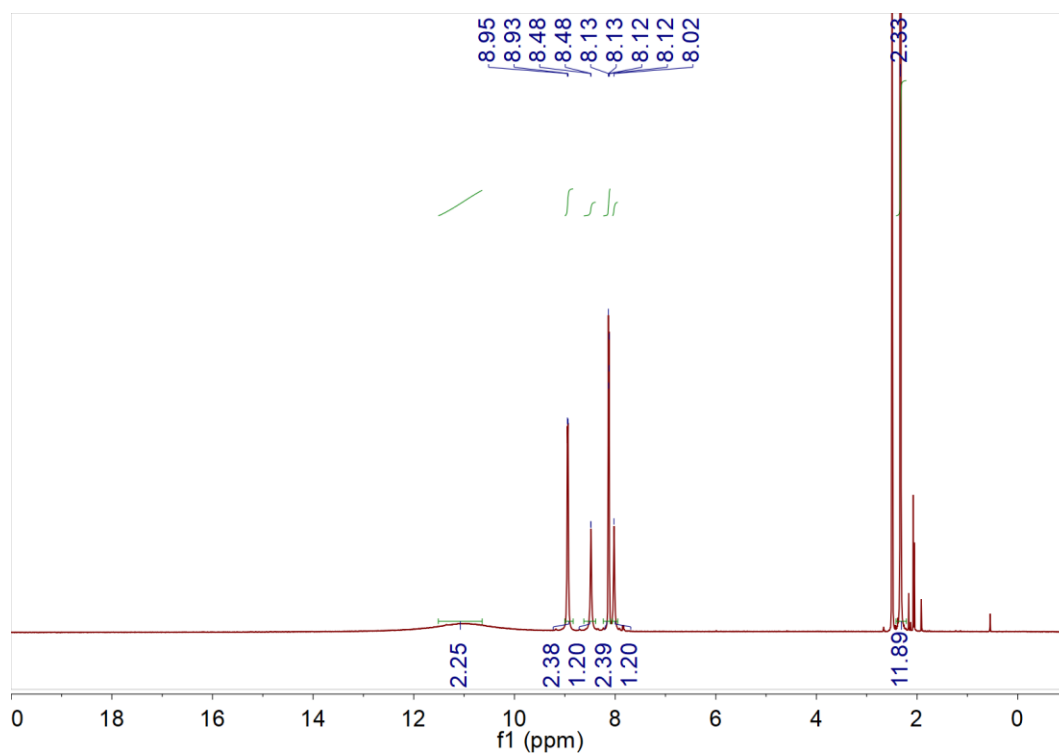


Figure S11. ^1H NMR of Co-6 in DMSO-d_6 .

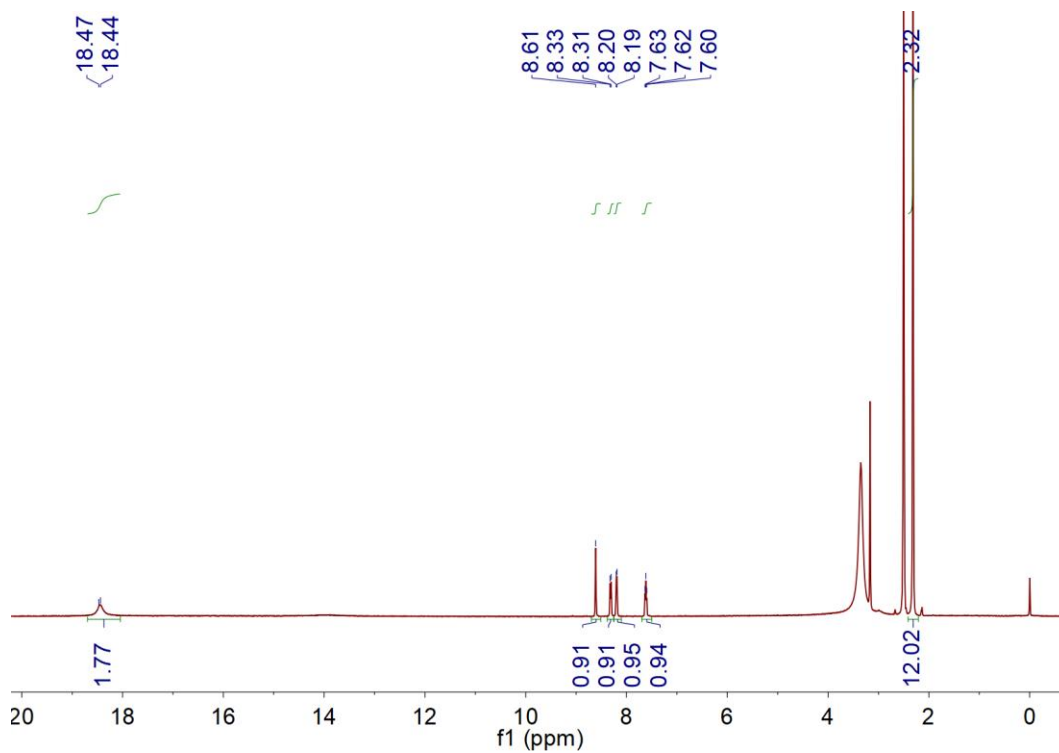


Figure S12. ^1H NMR of Co-7 in DMSO-d_6 .

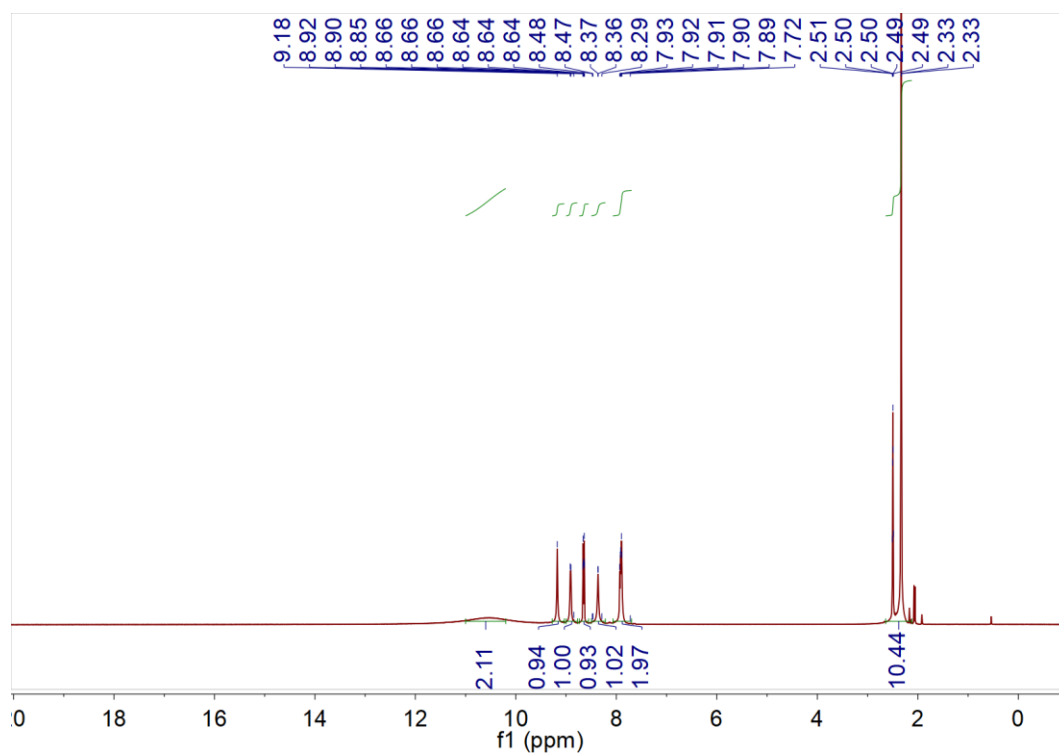


Figure S13. ^1H NMR of Co-8 in DMSO-d_6 .

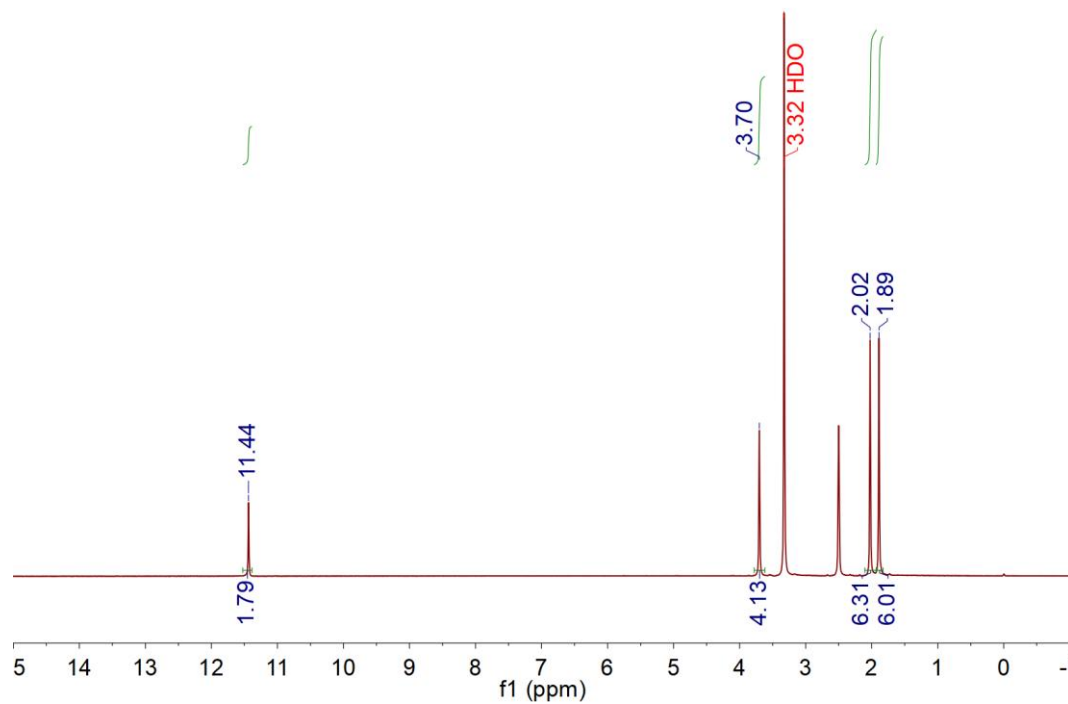


Figure S14. ^1H NMR of the $(\text{DOH})_2\text{en}$ ligand in DMSO-d_6 .

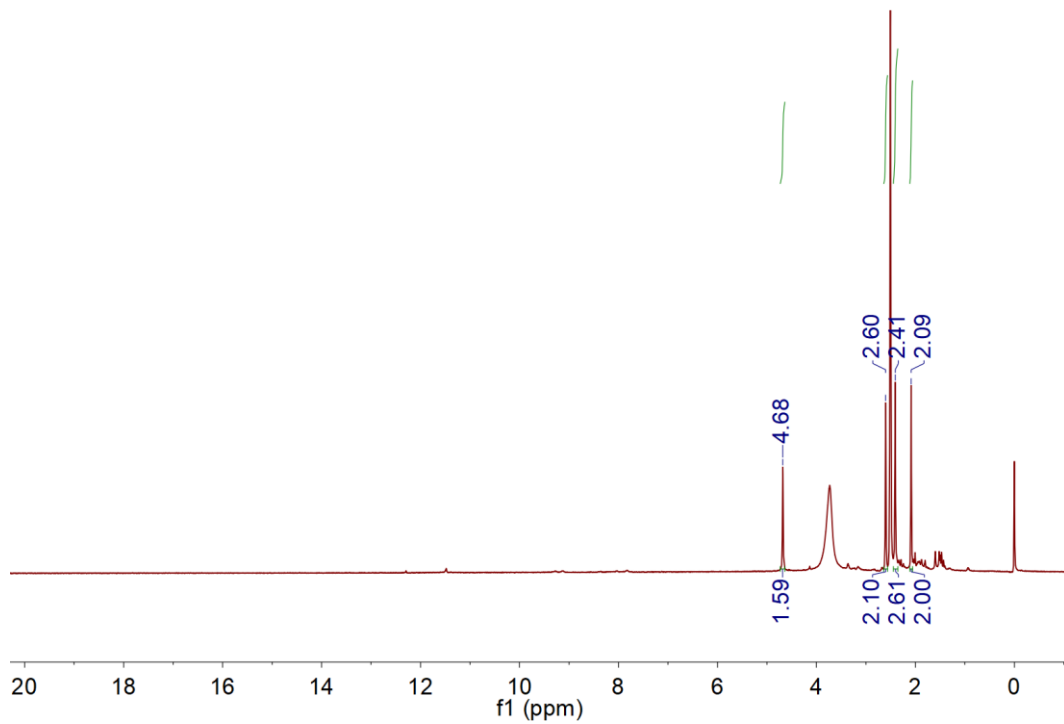


Figure S15. ^1H NMR of Co-9 in DMSO-d_6 .

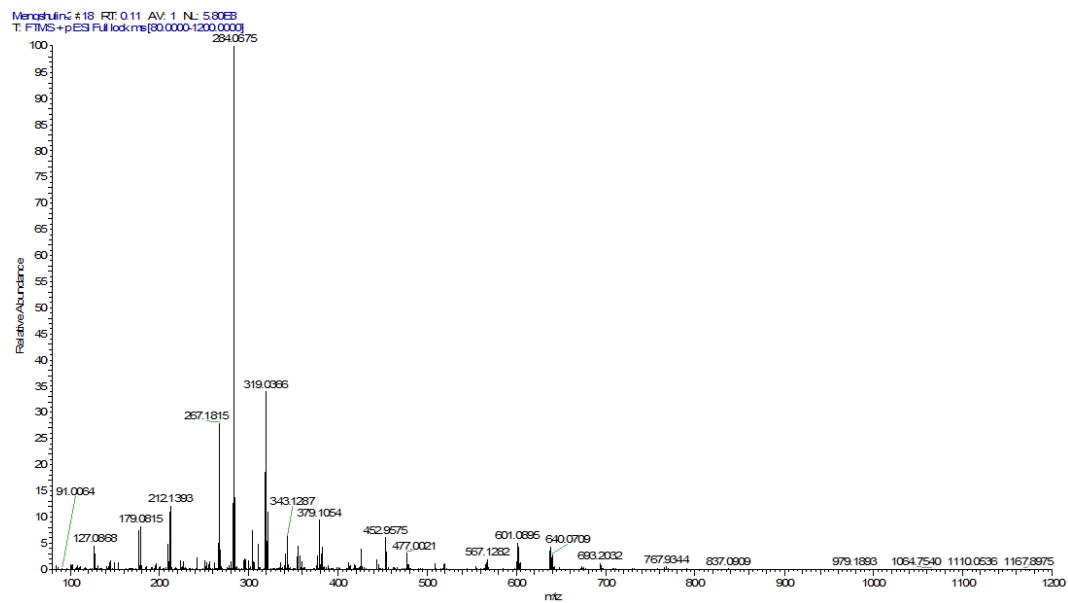


Figure S16. ESI-MS of Co-9.

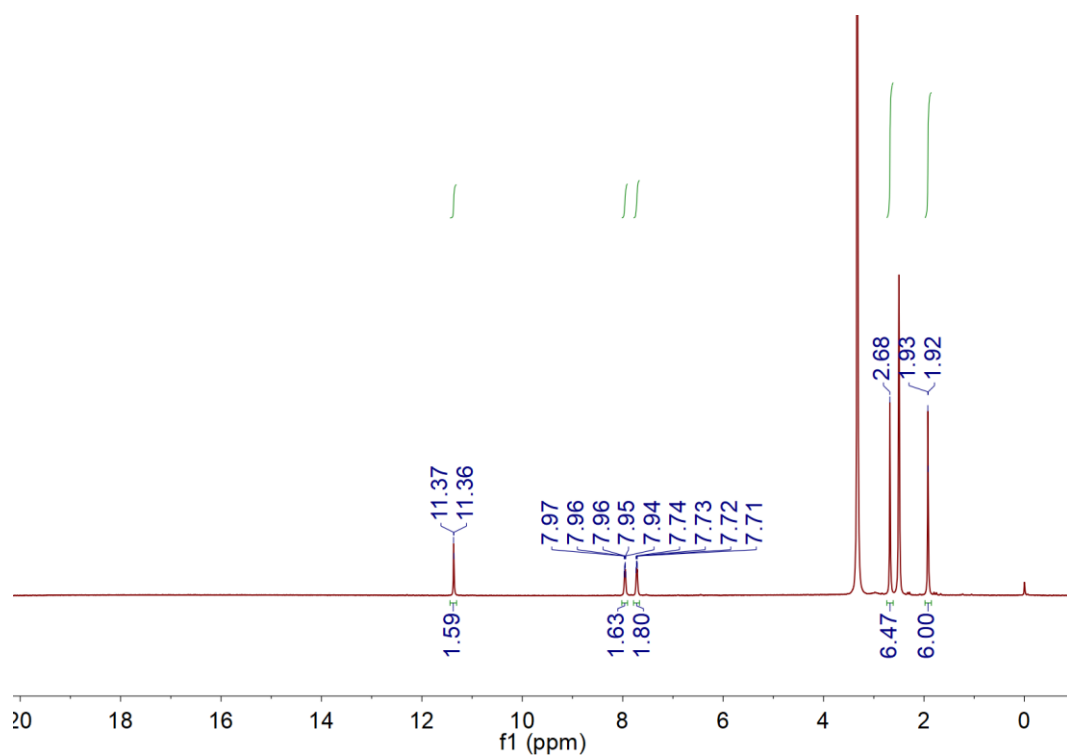


Figure S17. ^1H NMR spectrum of the $(\text{DOH})_2\text{Ph}$ ligand in DMSO-d_6 .

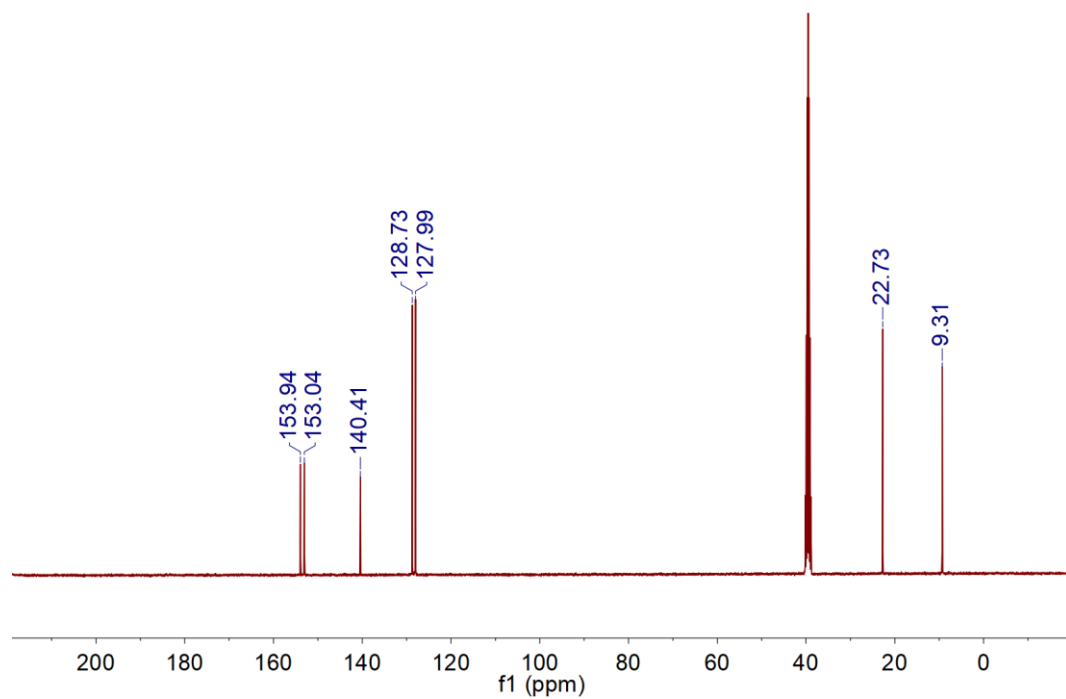


Figure S18. ^{13}C NMR spectrum of the $(\text{DOH})_2\text{Ph}$ ligand in DMSO-d_6 .

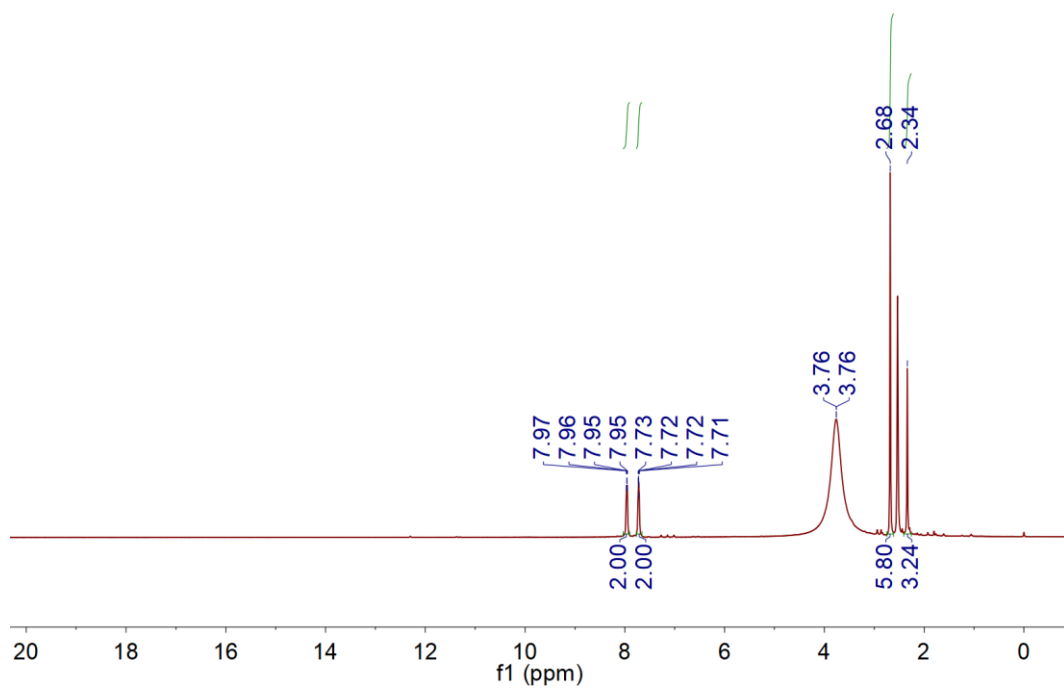


Figure S19. ^1H NMR of Co-10 in DMSO-d_6 .

3. Molecular eNO₂⁻RR chemistry

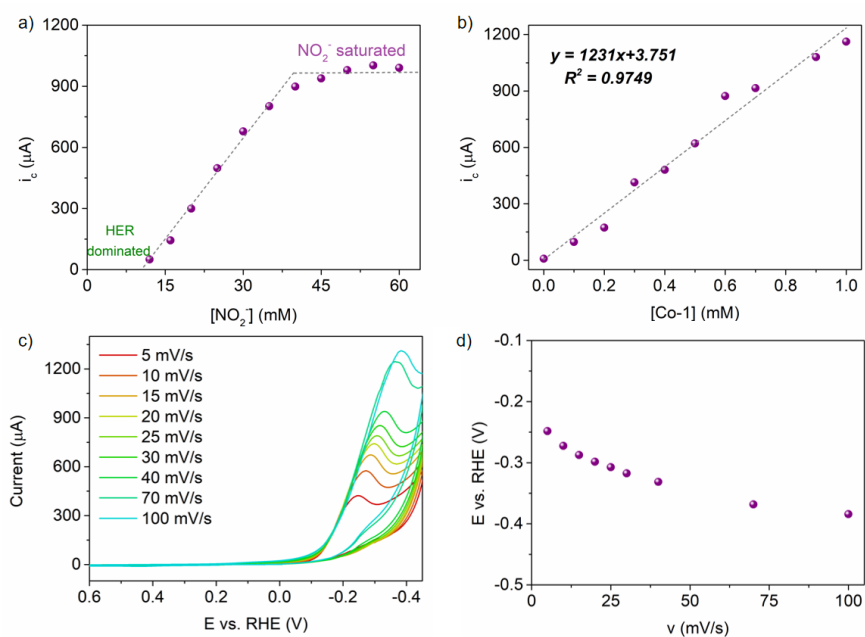


Figure S20. (a) The relationship of CV peak current against NO₂⁻ concentrations. (b) The relationship of CV peak current against Co-1 concentrations. (c) Cyclic Voltammetry of Co-1 with 50 mM NaNO₂ in pH = 6.7 Phosphate buffer at different scan rates. (d) The alternation of catalytic peak potentials over scan rates.

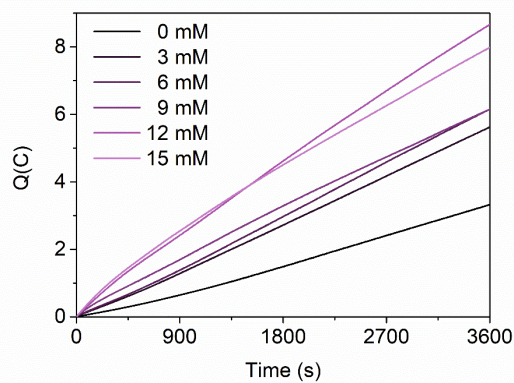


Figure S21. The CPE of complex Co-1 under different NaNO₂ concentrations. Conditions: 1 mM Co-1 + 0.5 M Na₂SO₄ + 0.25 M phosphate buffer (pH = 6.73) at -0.98 V vs. SCE (-0.34 V vs. RHE) for 3600 s.

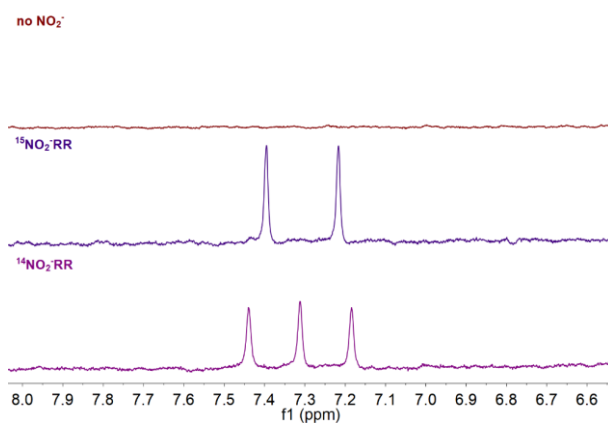


Figure S22. Measuring the NH_4^+ product by ^1H NMR in parallel $^{14}\text{NO}_2^-$ reduction and $^{15}\text{NO}_2^-$ reduction and in the absence of NO_2^- .

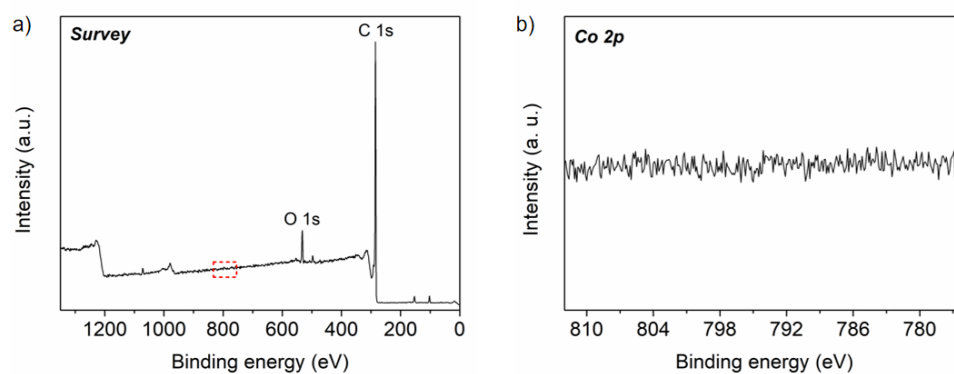


Figure S23. The (a) survey and (b) Co 2p XPS of the working electrode after electrocatalysis at -0.34 V vs. RHE (37 NO_2^- -to- NH_4^+ turnovers) using 1 mM Co-1 complex.

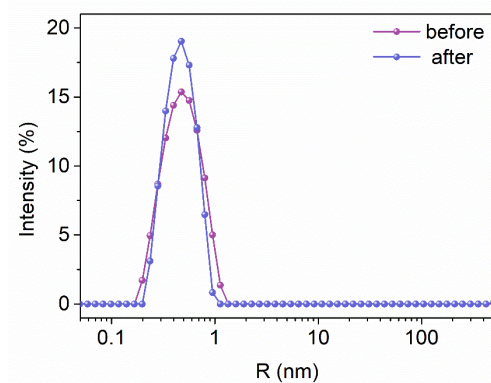


Figure S24. DLS showed no signs of particulate species after electrocatalytic NO_2^- reduction at -0.34 V vs. RHE using 1 mM Co-1 complexes.

Mengshulin-2 #18-19 RT: 0.10-0.11 AV: 2 NL: 1.32E8
T: FTMS + p ESI Full ms [50.0000-750.0000]

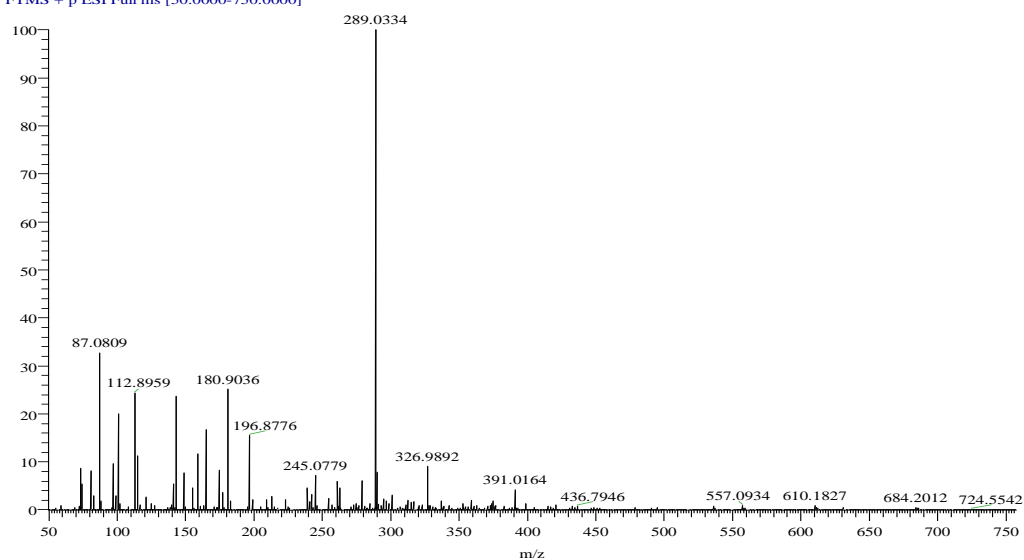


Figure S25. ESI-MS of Co-1 after electrolysis.

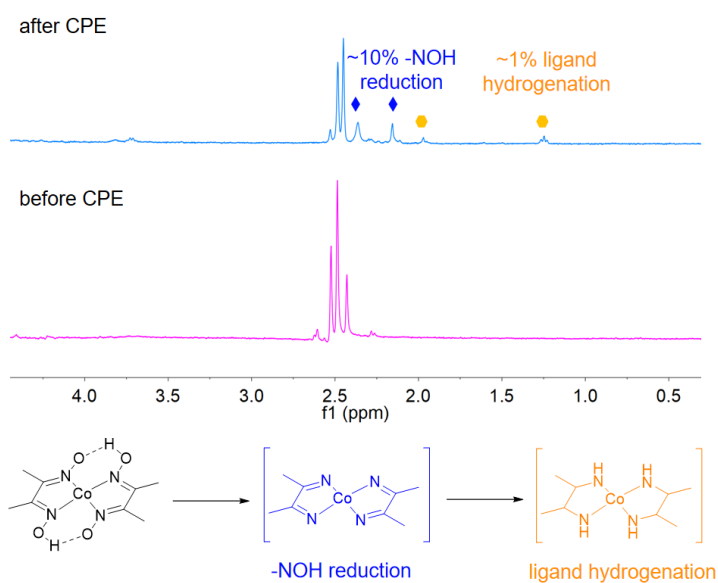


Figure S26. Comparison for the ^1H NMR spectra of Co-1 in D_2O before and after electrolysis (-0.37 V vs. RHE, 37 NO_2^- -to- NH_4^+ turnovers). Unlike in DMSO-d_6 , the $-\text{CH}_3$ signals for Co-1 in D_2O split into three singlets because the $-\text{OH}$ formed unsymmetric hydrogen bonds. Plausible structures and pathways for catalyst degradation are proposed based on NMR, which sum up $\sim 10\%$ of the original Co-1, showing that catalyst degradation was much slower than catalytic nitrite reduction.

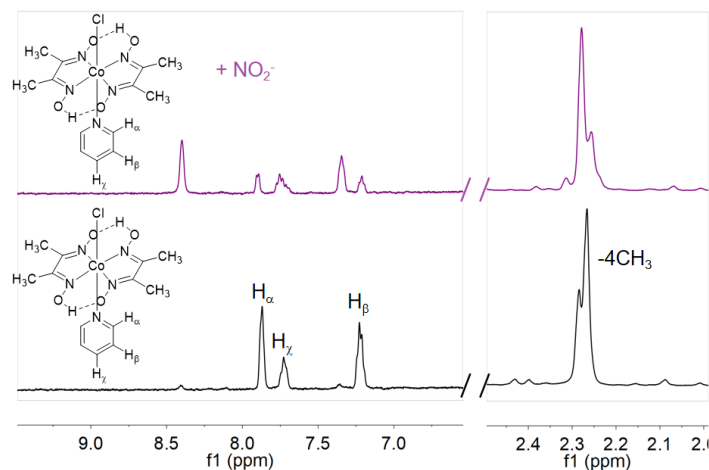


Figure S27. The ^1H NMR of Co-2 (5 mM) in D_2O with (30 mM) and without NO_2^- .

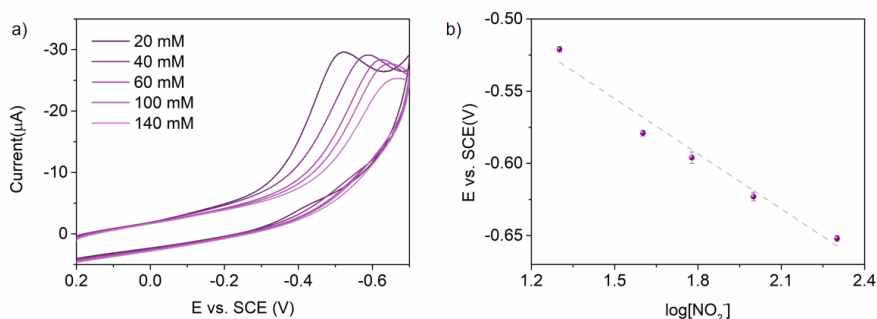
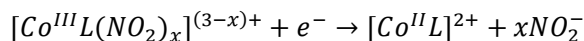


Figure S28. The $\text{Co}^{\text{III}}/\text{Co}^{\text{II}}$ reduction potential under different NO_2^- concentrations (a), which shows linear relationship between $\log[\text{NO}_2^-]$ with a slope of -126 mV/s (b).

In the presence of NO_2^- , the $\text{Co}^{\text{III}}/\text{Co}^{\text{II}}$ potential showed noticeable cathodic shift. According to Nernst equation, the $\text{Co}^{\text{III}}/\text{Co}^{\text{II}}$ potential has a linear relationship against the $\ln[\text{NO}_2^-]$:

$$E_{\text{Co}^{\text{III}}/\text{Co}^{\text{II}}} = E_{\text{Co}^{\text{III}}/\text{Co}^{\text{II}}}^0 - \frac{RT}{F} \ln([\text{NO}_2^-]^x) = E_{\text{Co}^{\text{III}}/\text{Co}^{\text{II}}}^0 - \frac{xRT}{F} \ln([\text{NO}_2^-])$$

which has a slope of $-59.2x \text{ mV/decade}$ when the $\text{Co}^{\text{III}}/\text{Co}^{\text{II}}$ event was correlated with the dissociation of $x \text{ NO}_2^-$ ligands:¹²



In Figure S28b, the $\text{Co}^{\text{III}}/\text{Co}^{\text{II}}$ potential followed a clear linear relationship ($R^2 = 0.966$) against $\log[\text{NO}_2^-]$ with a slope of -126 mV/pH , in good agreement with $x = 2$. The results suggested that the $\text{Co}^{\text{III}}/\text{Co}^{\text{II}}$ reduction event was accompanied with the dissociation of two NO_2^- ligands, showing that nitrite can occupy both the axial positions in Co-1.



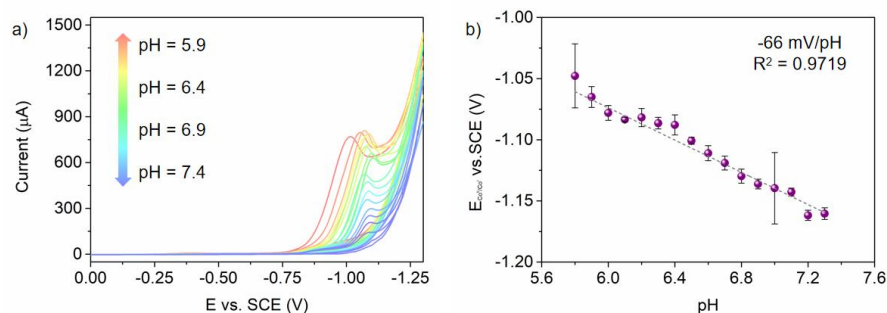


Figure S29. (a) CV of Co-1 with NO_2^- and different pH from 5.8 to 7.4. (b) The relationship between the peak potential and pH. Linear relationship between the peak potential and pH with a slope of -66 mV/pH indicated proton-coupled electron transfer with 1 H^+ per e^- nature.

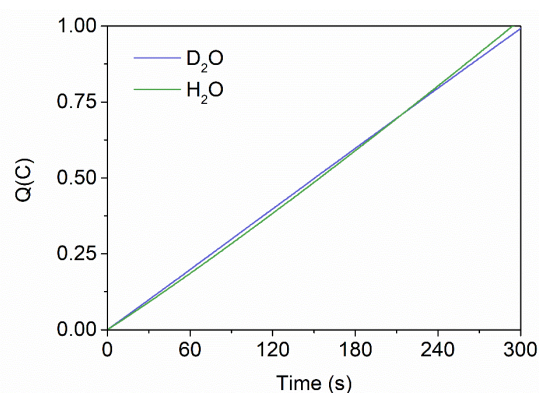


Figure S30. CPE of 1 mM Co-1 under standard conditions in H_2O and D_2O .

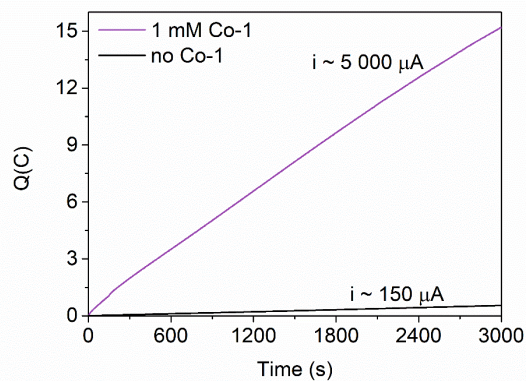


Figure S31. Electrocatalytic reduction of $\text{NO}(\text{g})$ at -0.34 V vs. RHE with and without Co-1.

For CPE with NO as N-substrate, the electrochemical cell was priorly degassed with Ar for 10 min and then bubbled with $\text{NO}(\text{g})$ for 10 min prepared in-situ, which was generated according to literature methods with FeSO_4 and NaNO_2 in water,¹³ and purified by passing the gas through deionized water to convert the generated NO_2 byproduct into NO . CPE followed standard testing procedures with $0.25 \text{ M Na}_2\text{SO}_4 + 0.25 \text{ M phosphate buffer (pH = 6.7)}$ under gas-tight conditions to avoid any NO re-oxidation that gave NO_x^- . In the presence of Co-1, NO reduction progressed steadily at $\sim 5 \text{ mA cm}^{-2}$, and after electrolysis, NH_4^+ was quantified by indophenol blue method as

the dominant product with 82% Faradic efficiency. In the absence of Co-1, bare glassy carbon electrode gave very sluggish NO (g) reduction current density of $\sim 0.15 \text{ mA cm}^{-2}$ with 26% Faradic efficiency for NH_4^+ . The results clearly present that Co-1 was active and necessary for NO-to- NH_4^+ transformation.

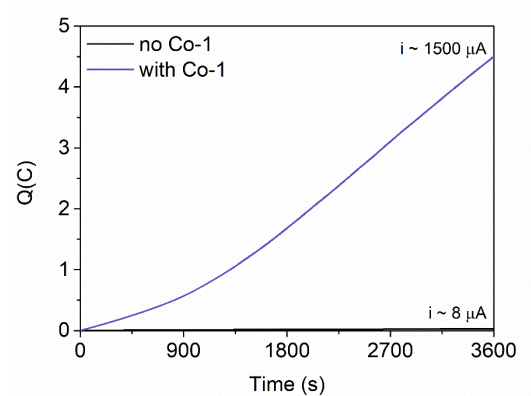


Figure S32. Electrocatalytic NH_2OH (10 mM) reduction at -0.34 V vs. RHE with and without Co-1. The minimal current in the absence of Co-1 demonstrated that the glassy carbon electrode alone was not active for the NH_2OH -to- NH_3 process, and Co-1 was necessary for NH_4^+ synthesis.

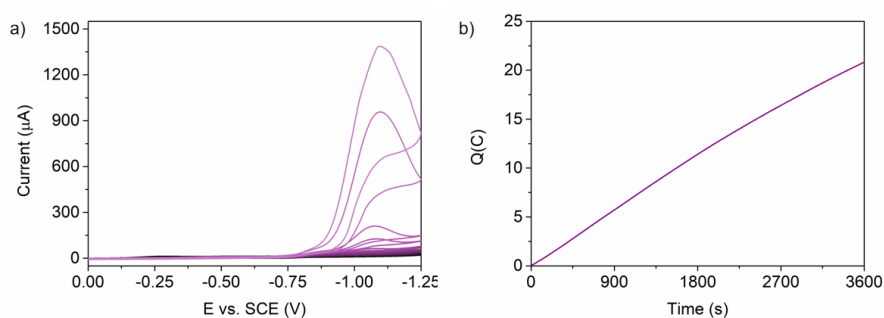


Figure S33. (a) CV of Co-2 (axial pyridine) under different NaNO_2 concentrations. (b) CPE of Co-2 for 1 h at -0.98 V vs. SCE with 50 mM NaNO_2 , $0.25 \text{ M Na}_2\text{SO}_4$ in 1:9 (v/v) DMSO- $0.25 \text{ M pH} = 6.7$ phosphate buffer.

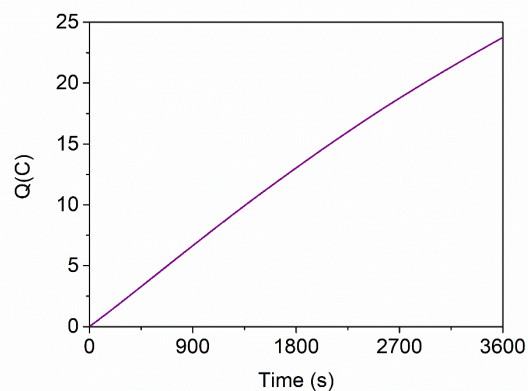


Figure S34. CPE of Co-3 (4-phenolpyridine as axial ligand) for 1 h at -0.98 V vs. SCE with 50 mM NaNO_2 , 0.25 M Na_2SO_4 in 1:9 (v/v) DMSO-0.25 M pH = 6.7 phosphate buffer.

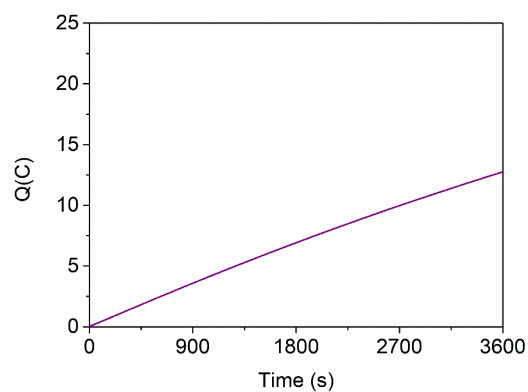


Figure S35. CPE of Co-4 (4-mercaptopyridine axial ligand) for 1 h at -0.98 V vs. SCE with 50 mM NaNO_2 , 0.25 M Na_2SO_4 in 1:9 (v/v) DMSO-0.25 M pH = 6.7 phosphate buffer.

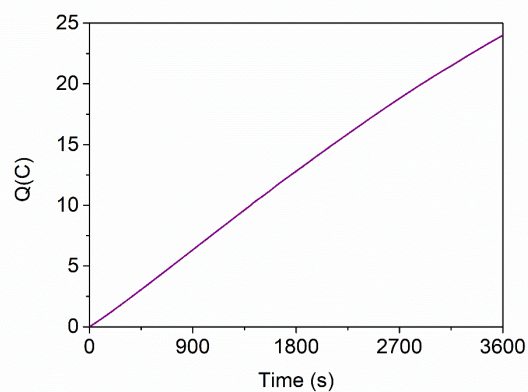


Figure S36. CPE of Co-5 (4-pyridinecarboxylic acid as axial ligand) for 1 h at -0.98 V vs. SCE with 50 mM NaNO_2 , 0.25 M Na_2SO_4 in 1:9 (v/v) DMSO-0.25 M pH = 6.7 phosphate buffer.

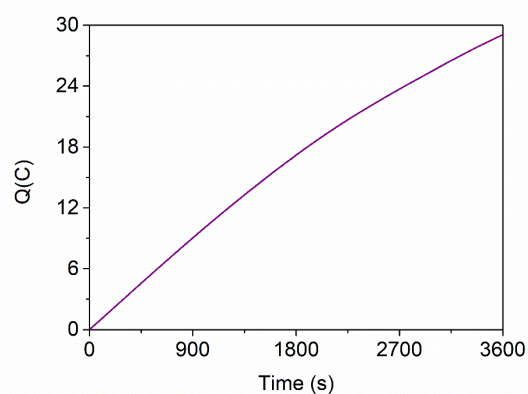


Figure S37. CPE of Co-6 (4-pyridinecarboxamide as axial ligand) for 1 h at -0.98 V vs. SCE with 50 mM NaNO₂, 0.25 M Na₂SO₄ in 1:9 (v/v) DMSO-0.25 M pH = 6.7 phosphate buffer.

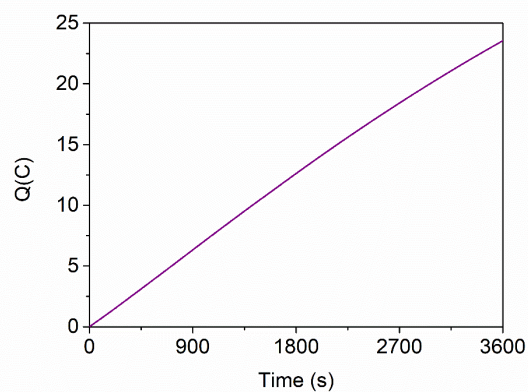


Figure S38. CPE of Co-7 (3-pyridinecarboxylic acid as axial ligand) for 1 h at -0.98 V vs. SCE with 50 mM NaNO₂, 0.25 M Na₂SO₄ in 1:9 (v/v) DMSO-0.25 M pH = 6.7 phosphate buffer.

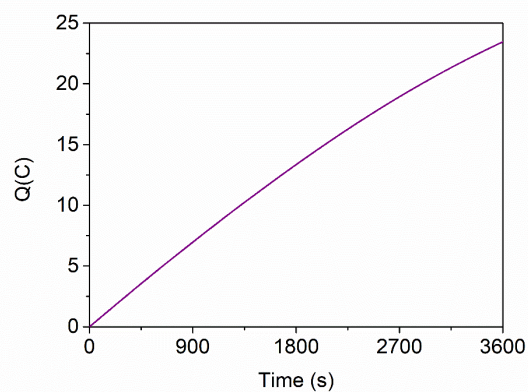


Figure S39. CPE of Co-8 (3-pyridinecarboxamide as axial ligand) for 1 h at -0.98 V vs. SCE with 50 mM NaNO₂, 0.25 M Na₂SO₄ in 1:9 (v/v) DMSO-0.25 M pH = 6.7 phosphate buffer.

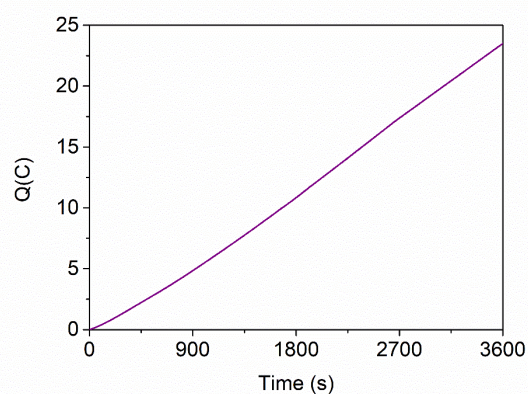


Figure S40. CPE of Co-9 (cobalt diimine-dioxime complex fused by $-\text{CH}_2\text{CH}_2-$) for 1 h at -0.98 vs. SCE with 50 mM NaNO_2 , $0.25 \text{ M Na}_2\text{SO}_4$ in $0.25 \text{ M pH} = 6.7$ phosphate buffer.

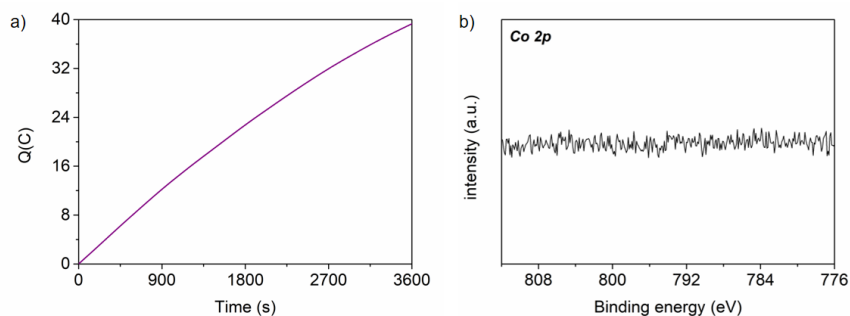


Figure S41. (a) CPE of Co-10 (cobalt diimine-dioxime complex fused by a benzene ring) for 1 h at -0.98 V vs. SCE with 50 mM NaNO_2 , $0.25 \text{ M Na}_2\text{SO}_4$ in $0.25 \text{ M pH} = 6.7$ phosphate buffer. (b) XPS of the working electrode after 1.0 h CPE with Co-10 showed no signs of Co particles.

Table S1. The electrocatalytic NO₂⁻-to-NH₃ reduction properties of cobaloxime complexes in this work in comparison with reported homogeneous complexes.

Catalyst	E. vs. SCE (V)	FE _{NH3} (%)	Ref.
Co-1~Co-10	-0.98	86-100	This work
CoGGH	-0.94	90	14
Co(DIM)	-1.05	88	15
FeN ₅ H ₂	-1.02	90 (NH ₂ OH) ^a	16
Co(CR)	-1.46	88	12
Fe(TMPyP)	-0.65	55-78 ^b	17
Co(cyclam)	-1.50	95 ^c	18
Ni(cyclam)	-1.50	95 ^c	18
CuPc	-1.54	78	19

Notes: a) further NH₂OH reduction to NH₄⁺ requires a Hg electrode

b) N₂O is formed as a major by-product

c) NH₄⁺ formation requires an Ag electrode.

4. eNO₂⁻RR with Cobaloxime-modified electrodes

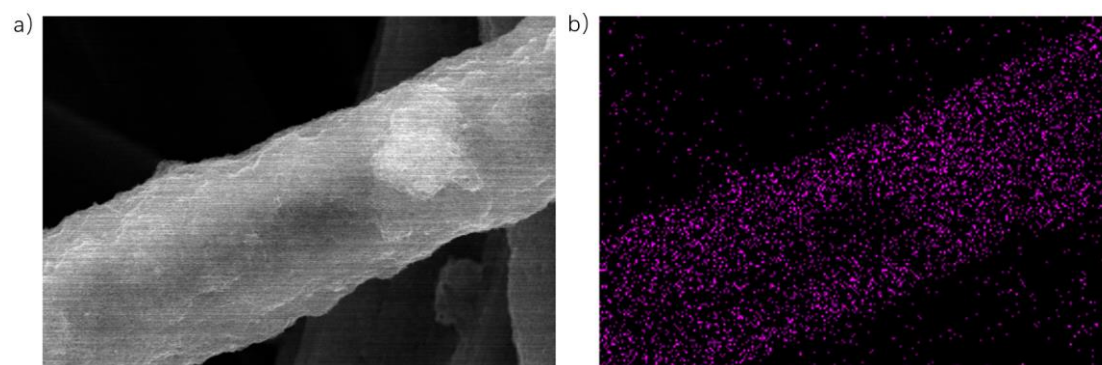


Figure S42. (a) Scanning electron microscopy (SEM) of as-prepared Co-1/CNT@CP electrodes with elemental mapping for Co (b).

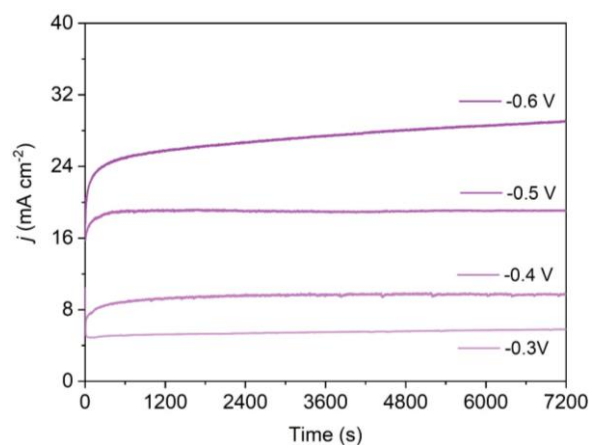


Figure S43. Chronoamperometry of Co-1/CNT@CP electrodes at different applied potentials.

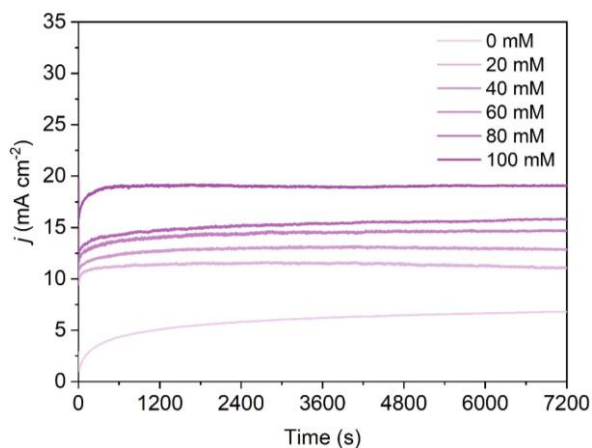


Figure S44. Chronoamperometry of Co-1/CNT@CP electrodes at different nitrite concentrations and -0.50 V vs. RHE for 2 h.

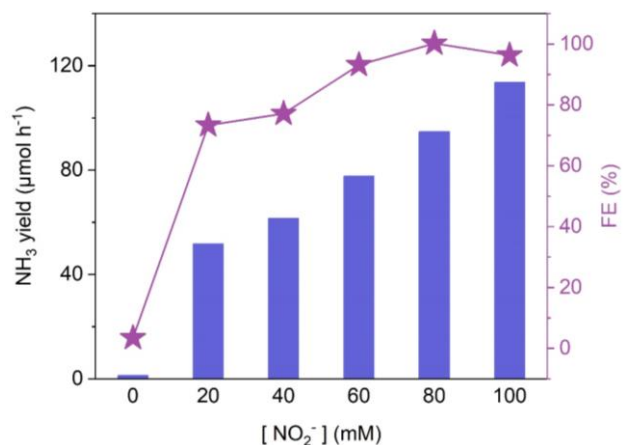


Figure S45. The ammonia yields and selectivities of Co-1/MWCNT@CP at variable NO₂⁻ concentrations.

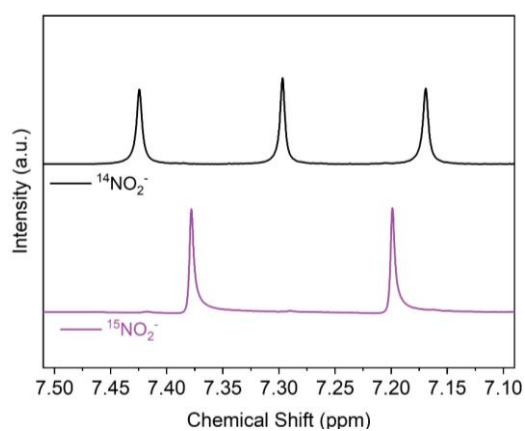


Figure S46. ¹H NMR signals for ¹⁵NH₄⁺ and ¹⁴NH₄⁺ after electrolysis of Co-1/CNT@CP electrode in ¹⁵NO₂⁻ and ¹⁴NO₂⁻ electrolytes.

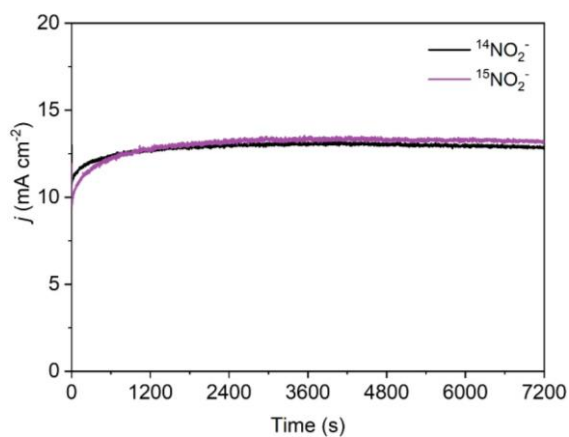


Figure S47. Chronoamperometry of Co-1/CNT@CP electrodes at -0.50 V vs. RHE in ¹⁴NO₂⁻ and ¹⁵NO₂⁻.

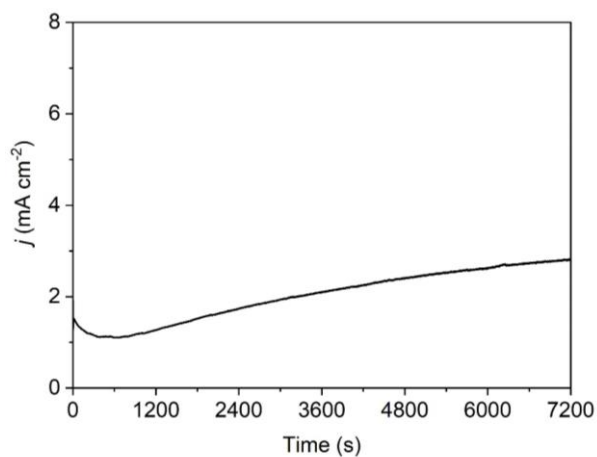


Figure S48. Chronoamperometry of CNT@CP electrodes absent of cobaloxime loading at -0.50 V vs. RHE in 100mM $^{14}\text{NO}_2^-$.

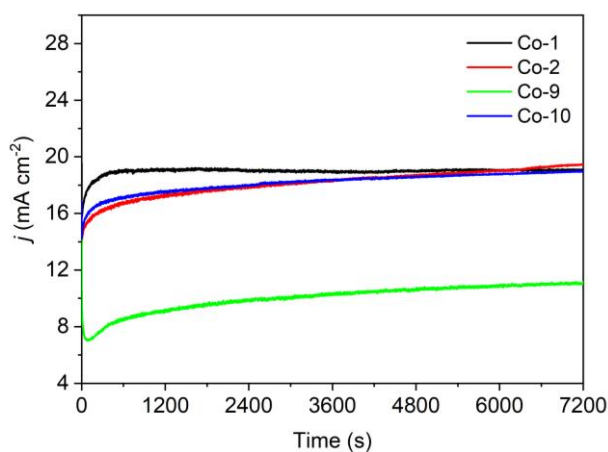


Figure S49. Chronoamperometry of Co-1/CNT@CP, Co-2/CNT@CP, Co-9/CNT@CP and Co-10/CNT@CP electrodes under standard conditions.

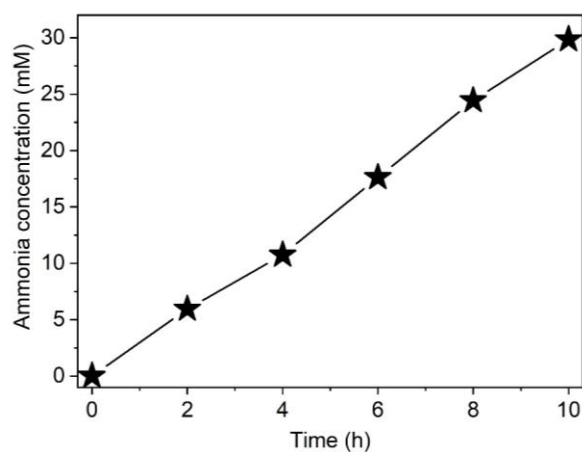


Figure S50. The ammonia concentration of Co-1/MWCNT@CP during consecutive 10 h electrolysis, with aliquots of sample taken every 2 hours for product quantification.

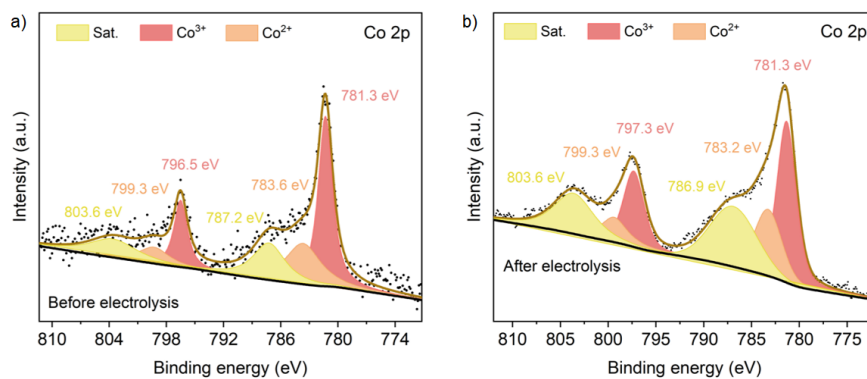


Figure S51. Co 2p XPS for Co-1/CNT@CP electrodes (a) before and (b) after 20 h electrolysis.

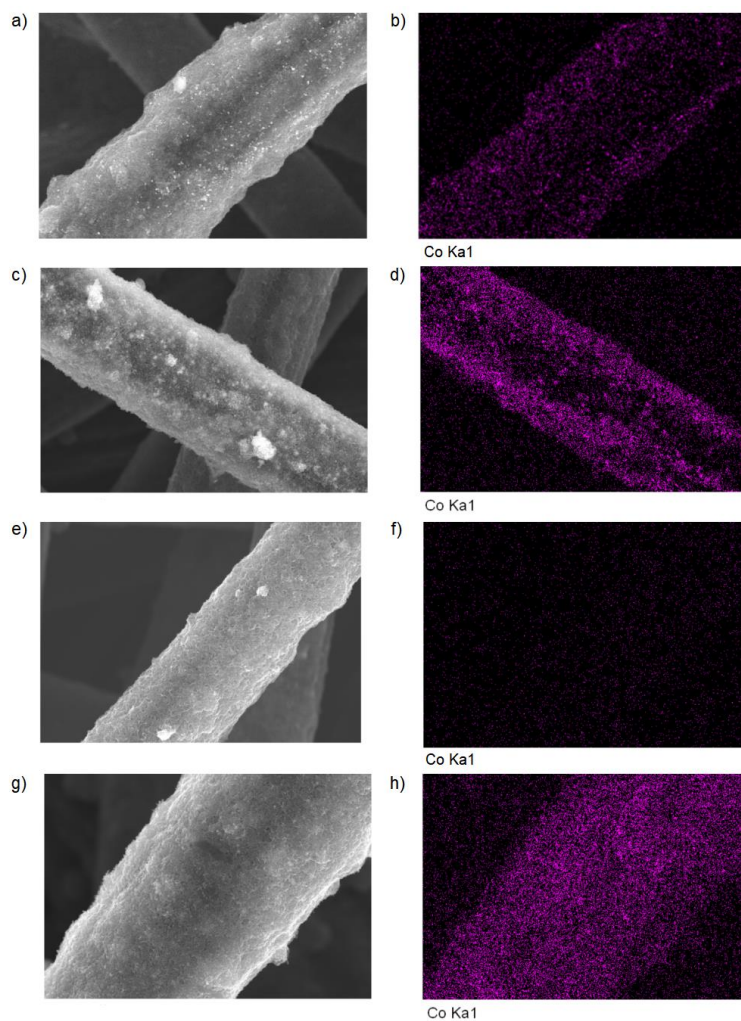


Figure S52. SEM and Co elemental mapping of Co-1/CNT@CP (a, b), Co-2/CNT@CP (c, d), Co-9/CNT@CP (e, f) and Co-10/CNT@CP (g, h) electrodes after electrolysis under standard conditions.

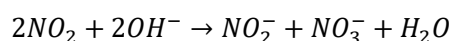
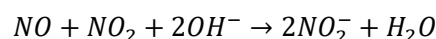
Table S2. Comparison of the mass-specific NO_x⁻ reduction performance for Co-n/CNT@CP with reported NO_x⁻ reduction electrocatalysts.

Catalyst	E vs. RHE(V)	NH ₃ yield (mg _{NH3} h ⁻¹ mg _{Cat} ⁻¹)	Ref.
Co-1/CNT@CP	-0.50	19.3	This work
Co-2/CNT@CP	-0.50	21.1	This work
Co-9/CNT@CP	-0.50	9.7	This work
Co-10/CNT@CP	-0.50	19.5	This work
Co@JDC/GF	-1.00	39.2	20
Ni ₃₅ -nanocrystal/SD	-0.50	11.0	21
CoP nanoarray/TM	-0.20	1.4	22
C/Co ₃ O ₄	-0.60	8.2	23
TiO _{2-x} nanobelt array/TP	-0.90	15.2	24
Fe SAC	-0.85	20.0	25
Fe-PPy SACs	-0.70	2.75	26
Fe-MoS ₂	-0.48	0.51 ^a	27
Fe-Mo-N-C SAC	-0.70	0.153	28
CoP NAs/CFC	-0.30	9.63	29

Note: a) area-specific activity.

5. Tandem plasma N₂ oxidation and eNO₂-RR

Plasma Nitrogen oxidation reaction (pNOR). According to literature reports with some modifications,³⁰ a high-voltage pulse generator (DP-2K, Henan Guangao Electronic Technology Co., Ltd, input voltage 5-9 V DC.) was used to activate N₂ and O₂, which was powered by 7.4 V 5600 mAh Li-ion batteries (Nanjing Nicjoy Electronic Technology Co., Ltd) or 9 V 10 W Si solar cells (P07-10, 35 cm × 23 cm, Fujian Zhugeliang Electronic Technology Co., Ltd). The high-voltage pulse generator outputs ~10 kV voltage, which was connected with two Cu wires with tips ~5 mm apart from each other, and put in a quartz tube (D = 24 mm, L = 150 mm) with an air inlet and gas outlet as the spark discharge reactor. Air at ambient temperature and pressure (78% N₂ and 21% O₂ by volume) was pumped into the reactor at 50 mL/min. The output gas mixture was led to a fresh 0.1 M NaOH trap (100 mL) to absorb as-generated NO_x:



The concentrations of as-obtained NO₂⁻ was measured by colorimetric method. In a typical measurement, 200 μL of the properly diluted absorbent was mixed with 1600 μL DI water, which was added 100 μL 1 wt% 4-aminobenzenesulfonic acid dissolved in 0.5 M H₂SO₄ and shaken vigorously for 5 min. Then, 100 μL 0.1 wt% aqueous solution of N-(1-Naphthyl) ethylenediamine dihydrochloride was added, and in the presence of NO₂⁻, the mixture turns magenta in 5 min upon vigorous shaking and displays an absorption peak at ~530 nm. The peak absorbance shows linear relationship with NO₂⁻ concentration (Figure S53).

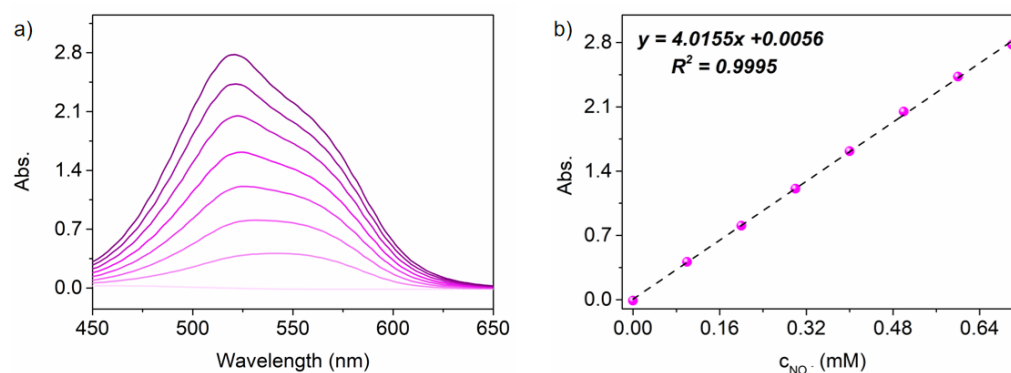


Figure S53. Determination of NO₂⁻ by colorimetric method.

The concentration of NO₃⁻ was measured by colorimetric method. One milliliter of properly diluted absorbent was mixed with 2 mL 0.8% sulfamic acid in 0.1 M HCl and shaken for 5 min. The

presence of NO_3^- causes significant increase of UV absorbances below 230 nm. By measuring the absorbances at 220 nm (A_{220}) and 275 nm (A_{275}), it was found that $A_{220}-2A_{275}$ displayed excellent linear relationship with NO_3^- concentrations with $R^2 = 0.9990$, as shown in Figure S54.

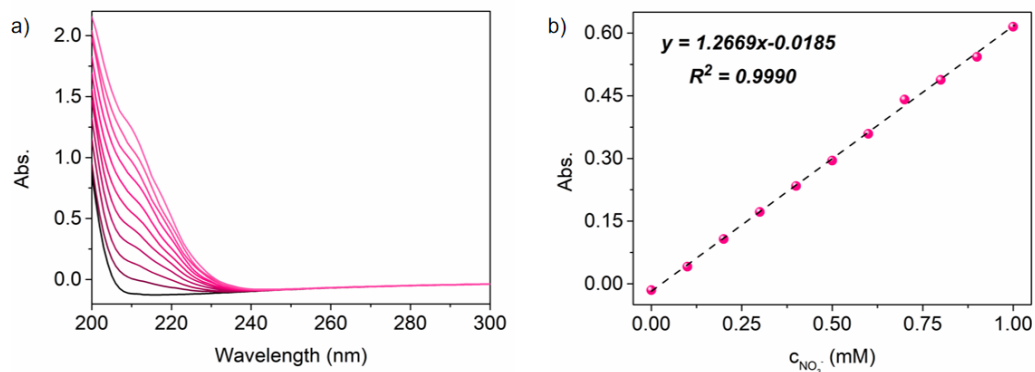


Figure S54. Determination of NO_3^- by UV absorption.

The as-obtained pNOR absorbent was stored in darkness and tuned to pH = 6.7 with NaH_2PO_4 before electrolysis.

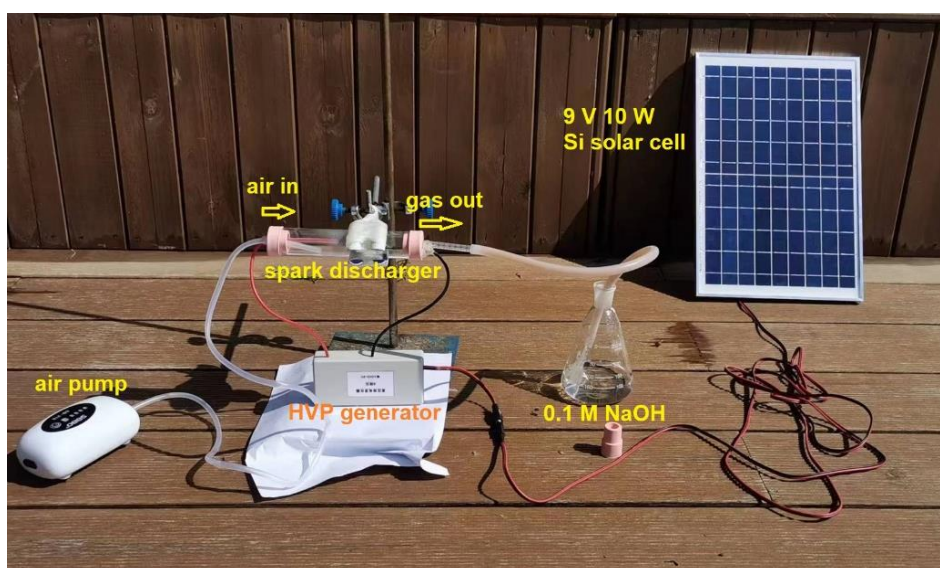


Figure S55. Photograph of the solar-driven pNOR device.

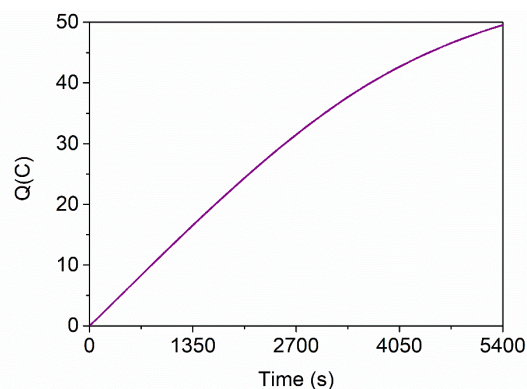


Figure S56. CPE of Co-1 with as-generated NO_x^- (51.6 mM) as the nitrogen source. The experiment was run under standard conditions, where the pH was tuned to 6.7 with NaH_2PO_4 .

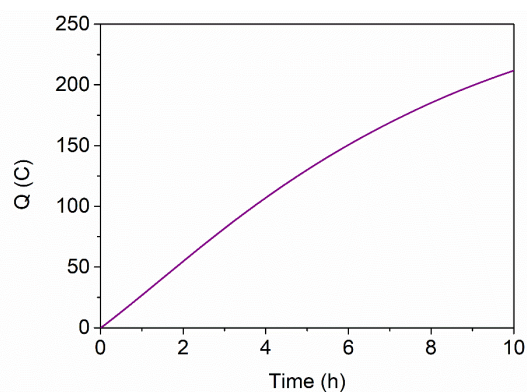


Figure S57. Chronoamperometry of Co-1/CNT@CP with NO_x^- (51.6 mM) generated by pNOR as the nitrogen source at -0.5 V vs. RHE and an initial pH of 6.7.

Table S3. Comparison of the mass-specific ammonia synthesis performance for Co-1/CNT@CP with reported ammonia synthesis methodologies and catalysts.

Catalyst	Method	NH_3 yield ($\text{mg}_{\text{NH}_3} \text{h}^{-1} \text{mg}_{\text{Cat}}^{-1}$)	Ref.
Co-1/CNT@CP	pNOR-eNO_2-RR	10.2^a	This work
$\text{Ru}_1/\text{N-C}$	e N_2 RR	1.21×10^{-1}	31
Fe_1/GDY	e N_2 RR	$(29.6 \pm 2.5) \times 10^{-2}$	32
$\text{Cu}^{\delta+}\text{-ZnAl LDH}$	photo- N_2 RR	1.87×10^{-3}	33
$\text{Bi}_5\text{O}_7\text{Br}$ nanotube	photo- N_2 RR	2.35×10^{-2}	34
$\text{Ba}_2\text{RuH}_6/\text{MgO}$	thermal- N_2 RR	1.01 (573K)	35
Co-LiH	thermal- N_2 RR	1.92×10^{-1} (623 K)	36

Note: a) adding together the time needed for both pNOR and e NO_2 -RR for a whole day-night cycle (24 h).

6. Reference

1. G. W. Watt and J. D. Chrisp, *Analytical Chemistry*, 1952, **24**, 2006-2008.
2. D. S. Frear and R. C. Burrell, *Analytical Chemistry*, 1955, **27**, 1664-1665.
3. R. Y. Hodgetts, A. S. Kiryutin, P. Nichols, H.-L. Du, J. M. Bakker, D. R. Macfarlane and A. N. Simonov, *ACS Energy Letters*, 2020, **5**, 736-741.
4. W. C. Trogler, R. C. Stewart, L. A. Epps and L. G. Marzilli, *Inorganic Chemistry*, 1974, **13**, 1564-1570.
5. A. Panagiotopoulos, K. Ladomenou, D. Sun, V. Artero and A. G. Coutsolelos, *Dalton Transactions*, 2016, **45**, 6732-6738.
6. Y. Xu, Y. Ye, T. Liu, X. Wang, B. Zhang, M. Wang, H. Han and C. Li, *Journal of the American Chemical Society*, 2016, **138**, 10726-10729.
7. J. Gu, Y. Yan, J. L. Young, K. X. Steirer, N. R. Neale and J. A. Turner, *Nature Materials*, 2016, **15**, 456-460.
8. E. Coropceanu, O. Bologa, I. Arsene, A. Vitiu, I. Bulhac, N. Gorinchiyo and P. Bourosh, *Russian Journal of Coordination Chemistry*, 2016, **42**, 516-538.
9. J. Wang, C. Li, Q. Zhou, W. Wang, Y. Hou, B. Zhang and X. Wang, *Dalton Transactions*, 2015, **44**, 17704-17711.
10. P.-A. Jacques, V. Artero, J. Pécaut and M. Fontecave, *Proceedings of the National Academy of Sciences*, 2009, **106**, 20627-20632.
11. V. V. Ramanujam and V. Alexander, *Inorganic Chemistry*, 1987, **26**, 3124-3134.
12. S. Partovi, Z. Xiong, K. M. Kulesa and J. M. Smith, *Inorganic Chemistry*, 2022, **61**, 9034-9039.
13. M. G. Suryaraman and A. Viswanathan, *Journal of Chemical Education*, 1949, **26**, 594.
14. Y. Guo, J. R. Stroka, B. Kandemir, C. E. Dickerson and K. L. Bren, *Journal of the American Chemical Society*, 2018, **140**, 16888-16892.
15. S. Xu, H.-Y. Kwon, D. C. Ashley, C.-H. Chen, E. Jakubikova and J. M. Smith, *Inorganic Chemistry*, 2019, **58**, 9443-9451.
16. J. R. Stroka, B. Kandemir, E. M. Matson and K. L. Bren, *ACS Catalysis*, 2020, **10**, 13968-13972.
17. M. H. Barley, M. R. Rhodes and T. J. Meyer, *Inorganic Chemistry*, 1987, **26**, 1746-1750.
18. I. Taniguchi, N. Nakashima, K. Matsushita and K. Yasukouchi, *Journal of Electroanalytical Chemistry and Interfacial Electrochemistry*, 1987, **224**, 199-209.
19. N. Chebotareva and T. Nyokong, *Journal of Applied Electrochemistry*, 1997, **27**, 975-981.
20. J. Wang, J. Liang, P. Liu, Z. Yan, L. Cui, L. Yue, L. Zhang, Y. Ren, T. Li, Y. Luo, Q. Liu, X.-E. Zhao, N. Li, B. Tang, Y. Liu, S. Gao, A. M. Asiri, H. Hao, R. Gao and X. Sun, *Journal of Materials Chemistry A*, 2022, **10**, 2842-2848.
21. P. Gao, Z.-H. Xue, S.-N. Zhang, D. Xu, G.-Y. Zhai, Q.-Y. Li, J.-S. Chen and X.-H. Li, *Angewandte Chemie International Edition*, 2021, **60**, 20711-20716.
22. G. Wen, J. Liang, Q. Liu, T. Li, X. An, F. Zhang, A. A. Alshehri, K. A. Alzahrani, Y. Luo, Q. Kong and X. Sun, *Nano Research*, 2022, **15**, 972-977.
23. R. Zhang, S. Zhang, Y. Guo, C. Li, J. Liu, Z. Huang, Y. Zhao, Y. Li and C. Zhi, *Energy & Environmental Science*, 2022, DOI: 10.1039/D2EE00686C.

24. D. Zhao, J. Liang, J. Li, L. Zhang, K. Dong, L. Yue, Y. Luo, Y. Ren, Q. Liu, M. S. Hamdy, Q. Li, Q. Kong and X. Sun, *Chemical Communications*, 2022, **58**, 3669-3672.
25. Z.-Y. Wu, M. Karamad, X. Yong, Q. Huang, D. A. Cullen, P. Zhu, C. Xia, Q. Xiao, M. Shakouri, F.-Y. Chen, J. Y. Kim, Y. Xia, K. Heck, Y. Hu, M. S. Wong, Q. Li, I. Gates, S. Siahrostami and H. Wang, *Nature Communications*, 2021, **12**, 2870.
26. P. Li, Z. Jin, Z. Fang and G. Yu, *Energy & Environmental Science*, 2021, **14**, 3522-3531.
27. J. Li, Y. Zhang, C. Liu, L. Zheng, E. Petit, K. Qi, Y. Zhang, H. Wu, W. Wang, A. Tiberj, X. Wang, M. Chhowalla, L. Lajaunie, R. Yu and D. Voiry, *Advanced Functional Materials*, **n/a**, 2108316.
28. E. Murphy, Y. Liu, I. Matanovic, S. Guo, P. Tieu, Y. Huang, A. Ly, S. Das, I. Zenyuk, X. Pan, E. Spoerke and P. Atanassov, *ACS Catalysis*, 2022, **12**, 6651-6662.
29. S. Ye, Z. Chen, G. Zhang, W. Chen, C. Peng, X. Yang, L. Zheng, Y. Li, X. Ren, H. Cao, D. Xue, J. Qiu, Q. Zhang and J. Liu, *Energy & Environmental Science*, 2022, DOI: 10.1039/D1EE03097C.
30. Y. Ren, C. Yu, L. Wang, X. Tan, Z. Wang, Q. Wei, Y. Zhang and J. Qiu, *Journal of the American Chemical Society*, 2022, **144**, 10193-10200.
31. Z. Geng, Y. Liu, X. Kong, P. Li, K. Li, Z. Liu, J. Du, M. Shu, R. Si and J. Zeng, *Advanced Materials*, 2018, **30**, 1803498.
32. Y. Fang, Y. Xue, L. Hui, H. Yu and Y. Li, *Angewandte Chemie International Edition*, 2021, **60**, 3170-3174.
33. S. Zhang, Y. Zhao, R. Shi, C. Zhou, G. I. N. Waterhouse, L.-Z. Wu, C.-H. Tung and T. Zhang, *Advanced Energy Materials*, 2020, **10**, 1901973.
34. S. Wang, X. Hai, X. Ding, K. Chang, Y. Xiang, X. Meng, Z. Yang, H. Chen and J. Ye, *Advanced Materials*, 2017, **29**, 1701774.
35. Q. Wang, J. Pan, J. Guo, H. A. Hansen, H. Xie, L. Jiang, L. Hua, H. Li, Y. Guan, P. Wang, W. Gao, L. Liu, H. Cao, Z. Xiong, T. Vegge and P. Chen, *Nature Catalysis*, 2021, **4**, 959-967.
36. P. Wang, F. Chang, W. Gao, J. Guo, G. Wu, T. He and P. Chen, *Nature Chemistry*, 2017, **9**, 64-70.